Electrochimica Acta 404 (2022) 139764

Contents lists available at ScienceDirect

Electrochimica Acta

journal homepage: www.elsevier.com/locate/electacta

Physics-based modeling of sodium-ion batteries part II. Model and validation

Kudakwashe Chayambuka[a,b,c], Grietus Mulder[b,c], Dmitri L. Danilov[a,d], Peter H.L. Notten[a,d,e,*]

[a] Eindhoven University of Technology, P.O. Box 513, 5600MB Eindhoven, the Netherlands
[b] VITO, Boeretang 200, 2400 Mol, Belgium
[c] EnergyVille, Thor Park 8310, 3600 Genk, Belgium
[d] Forschungszentrum Jülich, Fundamental Electrochemistry (IEK-9), D-52425 Jülich, Germany
[e] Centre for Clean Energy Technology, University of Technology Sydney, Broadway, Sydney, NSW, 2007, Australia

ARTICLE INFO

Article history:
Received 14 July 2021
Revised 12 December 2021
Accepted 16 December 2021
Available online 19 December 2021

Keywords:
Sodium-ion batteries
P2D Model
Physics-based model
NVPF
HC
Genetic algorithm
Reference electrode
Anode potential
Ragone plot

ABSTRACT

Sodium-ion batteries (SIBs) have recently been proclaimed as the frontrunner 'post lithium' energy storage technology. This is because SIBs share similar performance metrics with lithium-ion batteries, and sodium is 1000 times more abundant than lithium. In order to understand the electrochemical characteristics of SIBs and improve present-day designs, physics-based models are necessary. Herein, a physics-based, pseudo-two-dimensional (P2D) model is introduced for SIBs for the first time. The P2D SIB model is based on $Na_3V_2(PO_4)_2F_3$ (NVPF) and hard carbon (HC) as positive and negative electrodes, respectively. Charge transfer in the NVPF and HC electrodes is described by concentration-dependent diffusion coefficients and kinetic rate constants. Parametrization of the model is based on experimental data and genetic algorithm optimization. It is shown that the model is highly accurate in predicting the discharge profiles of full cell HC//NVPF SIBs. In addition, internal battery states, such as the individual electrode potentials and concentrations, can be obtained from the model at applied currents. Several key challenges in both electrodes and the electrolyte are herein unraveled, and useful design considerations to improve the performance of SIBs are highlighted.

1. Introduction

Several research groups and startups have recently shown great interest in developing sodium-ion batteries (SIBs) [1]. SIBs are, at present, regarded as the most promising complementary technology to the ubiquitous lithium-ion batteries (LIBs) [2]. This is because sodium is 1000 times more abundant than lithium on the earth's crust [3,4]. In addition, both battery types share similarities in performance, physical structure, and manufacturing infrastructure. As a result, the scientific knowledge and know-how accumulated in developing LIBs have been transferred in the past decade to accelerate the commercialization efforts of SIBs [5]. The most encouraging outcome of this recent drive is the availability of a large repository of cathode material choices for SIB applications, all of which are based on earth-abundant elements [3]. Therefore, while LIBs are expected to continue to dominate in the mass markets of electric vehicles [6,7], the SIB technology is expected to leverage its resource abundance and provide sustainable energy storage solutions in large-scale stationary applications [8].

The development of a new battery chemistry, such as the SIB, and the design of control algorithms for battery management systems (BMSs) is also dependent on accurate, physics-based models. Such models give reliable information regarding the performance of battery electrodes, thus enabling design improvements and performance benchmarking. The development of physics-based models for porous insertion electrodes can be traced to the pioneering work of West *et al.* [9] in the early 1980^s. This period incidentally coincided with the 'rocking chair' battery design, in which two insertion electrodes were used in commercial cells instead of metallic lithium anodes for safety reasons [10]. West's model described the coupled transport of ionic species in the electrolyte and electrode phases using the principles of the porous electrode theory, a theory which had been developed by Newman et al. [11]. However, West's model conceptualized a porous electrode as a

* Corresponding author.
E-mail address: p.h.l.notten@tue.nl (P.H.L. Notten).

https://doi.org/10.1016/j.electacta.2021.139764

monolithic slab with straight pores and high conductivity. Newman *et al.* [12,13] later improved this simplified model structure by treating electrode particles as a distinct phase in intimate contact with the electrolyte. Using the principles of homogenization, the particles were treated as a macro-homogeneous phase. Newman's model, therefore, provided the basic framework for the rigorous treatment of charge transport in discrete and conceptually spherical electrode particles. This multi-phase, multi-scale coupling is often referred to as the pseudo-two-dimensional (P2D) model structure because of the 1D representation of the electrode thickness and an additional, pseudo-dimension, representing the spherical radius of active particles at different electrode positions.

Various P2D models have been applied to different battery chemistries, such as lead-acid and nickel-metal hydride [14,15]. Although P2D models are widely accepted and demonstrate unparalleled accuracy and reliability, there remain practical challenges to parametrize new chemistries and integrate the models in BMS microcontrollers [16]. This is because the models are based on systems of coupled partial differential equations (PDEs), which are computationally expensive and potentially non-convergent during execution [17]. This fundamental challenge has propelled a growing trend of using reduced-order models such as single-particle models [18–20], equivalent circuit models [21,22], and data-driven semi-empirical models [23,24].

Details of the reduced-order battery models have been published in thematic reviews for the interested reader [25,26]. Nevertheless, as models become increasingly simplified, the danger is obtaining parameters that are detached from electrochemistry and physics. In the end, the simplified models cannot be reliably used as predicting tools to improve cell design because the underlying parameters lack physical meaning and are not valid outside the conditions of model parametrization. Therefore, the development of physics-based models remains an important undertaking to understand internal battery dynamics and provide a link with experimentally derived parameters. This development should carefully consider all relevant electrochemical processes involved in the given battery chemistry to achieve an accurate physical model.

Herein, a physics based, P2D model of a SIB full cell is presented for the first time to understand and improve the design of this emerging battery chemistry. The experiments used to derive parameters of a SIB based on hard carbon (HC) as the anode/negative electrode and $Na_3V_2(PO_4)_2F_3$ (NVPF) as cathode/positive electrode are described in a separate, preceding paper [27]. The electrolyte is composed of 1 kmol m^{-3} $NaPF_6$ salt dissolved in equal weight mixtures of ethylene carbonate (EC) and propylene carbonate (PC), $EC_{0.5} : PC_{0.5}$ (w/w) solvent. Based on the experimental evidence, the SIB electrode and electrolyte parameters are concentration-dependent. As a result, concentration-dependent diffusion coefficients, kinetic rate constants, and conductivity are introduced to the P2D model.

The full cell SIB model is scripted in MATLAB, which disposes of a global optimization toolbox to determine parameters that could not be experimentally deduced. Using the genetic algorithm for the optimization procedure, the SIB model is validated by comparing the simulation results with experimental voltage data for the positive and negative electrode potentials. Analyses of the model results reveal mass transport limitations in the 1 kmol m^{-3} $NaPF_6$ $EC_{0.5} : PC_{0.5}$ (w/w) electrolyte and in the HC and NVPF active particles. This can further guide the design of SIB systems, which are expected to operate at high-power demanding applications.

2. Description of the system components

Fig. 1 shows a detailed layout of a three-electrode SIB setup composed of an HC negative electrode, a separator, an NVPF positive electrode, and a metallic sodium reference electrode (Na-RE). These are assembled in a PAT-Cell (EL-Cell GmbH). HC and NVPF electrodes, in this case, act as two working electrodes, and the Na-RE acts as reference electrode of the first kind. The Na-RE is carefully positioned between the two working electrodes for accurate potential measurements while being electronically isolated from either electrode by the separator.

The thickness of the negative electrode, the separator, and the positive electrode are $\delta_n = 64$, $\delta_s = 25$ and $\delta_p = 68$ [µm], respectively. Based on experimental scanning electron micrographs, the average radii of the HC and NVPF electrode particles are $R_n = 3.48$ and $R_p = 0.59$ [µm], respectively [27]. R_n is, therefore, 6 times larger than R_p on average. Both electrodes additionally contain graphitic conductive additives in order to enhance the electrical conductivity of the composite electrodes. These are represented in Fig. 1 by the black spheres. More conductive additives are needed in the NVPF positive electrode because of the low electronic conductivity of the NVPF material [28,29].

Fig. 1 also shows the cable connections from the potentiostat to the three electrodes for automated cycling and cell voltage measurements. A current I_{app} [A] is specified in the potentiostat program to either charge or discharge the SIB. The Na-RE is connected to a high impedance lead of the potentiostat, which ensures a very low current passes through the RE. The three-electrode setup, therefore, allows for the accurate determination of individual electrode potentials *vs.* Na-RE. As a result, positive electrode potential (V_p), and the negative electrode potential (V_n), can be deconvoluted from the full cell voltage (V_{bat}) at different values of I_{app}.

From a modeling perspective, this knowledge of the individual electrode potentials is important for two reasons. First, the parameters for both electrodes can be independently optimized instead of relying only on V_{bat}, which is a combination of the two electrode potentials. In this way, parameters for the individual electrodes can be independently optimized. Second, the number of simultaneously optimized parameters is reduced, which increases optimization speed and model fidelity. Care, however, must be exercised on the position of the reference electrode to minimize overpotentials and voltage crosstalk between the anode and the cathode.

3. Model description

In the isothermal P2D model described herein, the active particles are considered spherical. Another assumption is that the particle sizes are homogeneous and represented by the average particle radius. The model variables include the Na-concentration ($c_{\theta,m}$), the potential ($\varphi_{\theta,m}$), and current ($i_{\theta,m}$). The subscript θ symbolizes the phase of the variable, which can either be the solid phase ($\theta = 1$) or the liquid/electrolyte phase ($\theta = 2$), subscript m symbolizes the domain inside the battery stack, which can either be the negative electrode ($m = n$), the positive electrode ($m = p$) or the separator ($m = s$).

3.1. Mass transport in electrode particles

Fick's second law expresses the time-dependent radial transport of intercalated Na^+ inside the electrode active particles

$$\frac{\partial c_{1,m}}{\partial t} = \frac{1}{r_m^2}\frac{\partial}{\partial r_m}\left(D_{1,m}\, r_m^2\, \frac{\partial c_{1,m}}{\partial r_m}\right), \quad \forall t, \quad m = \{n, p\}, \quad 0 \le r_m \le R_m, \tag{1}$$

where $c_{1,m}$ is the concentration of the intercalated Na^+ [mol m^{-3}], $D_{1,m}$ is the solid-state diffusion coefficient [$m^2 s^{-1}$], r_m is the particle radius [m], and t is time [s]. At the particle surface ($r_m = R_m$) and at the center ($r_m = 0$), the flux/Neumann boundary conditions

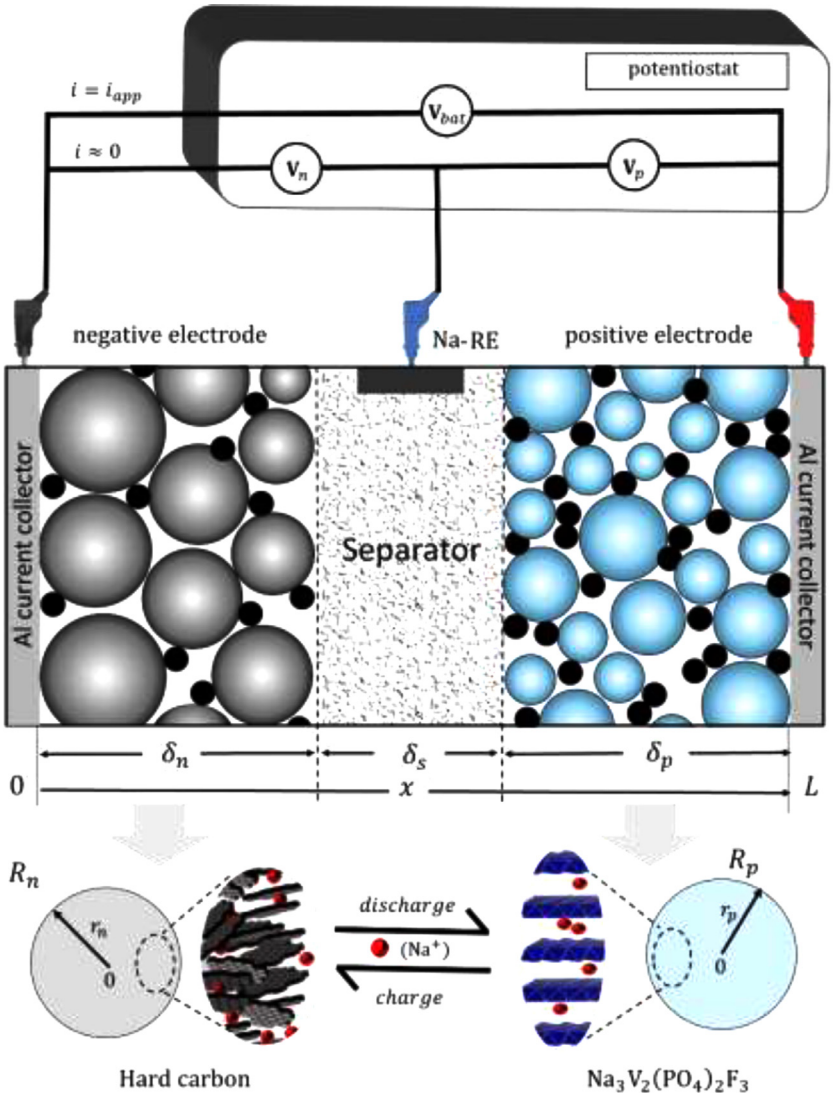

Fig. 1. HC//NVPF full cell configuration and potentiostat connections to the microporous battery SIB electrodes.

are applied to Eq. (1), implying

$$-D_{1,m}\frac{\partial c_{1,m}}{\partial r_m}|_{r_m=R_m} = j_m,\ \ m = \{n, p\} \tag{2}$$

$$\frac{\partial c_{1,m}}{\partial r_m}|_{r_m=0} = 0,\ \ m = \{n, p\} \tag{3}$$

where j_m is the interfacial flux of species [mol m^{-2} s^{-1}]. The boundary conditions in Eqs. (2) and 3 express the surface reaction flux and spherical symmetry, respectively. An initial condition is further required for the particle phase concentrations, which is defined as

$$c_{1,m}(r, t = 0) = \ c^0_{1,m},\ \ m = \{n, p\} \tag{4}$$

where $c^0_{1,m}$ is the initial Na^+ concentration inside electrode particles. $c^0_{1,m}$ depends on the initial state-of-charge (SOC) of the active materials.

In the case of Na^+ intercalation with constant $D_{1,m}$ and R_m, Eqs. (1) to 4 can be solved by fast analytical methods [30,31]. R_m changes in intercalation active materials are generally very low. In the case of NVPF and HC electrode materials, unit cell volume changes of approximately 2% have been reported [32]. However, experimental and modeling galvanostatic intermittent titration technique (GITT) results showed that $D_{1,m}$ is strongly dependent on $c_{1,m}$ [27,33,34]. In other studies, $D_{1,p}$ has also been shown to vary by two orders of magnitude [33]. For this reason, a concentration-dependent $D_{1,m}$ is used for the NVPF//HC SIB. As a result, the numerical method of the hybrid backward Euler control volume method (HBECV) is applied instead of the analytical methods. The HBECV obtains fast and accurate solutions and has been reported before elsewhere [35].

3.2. Electrode kinetics model

At the particle surface, the electrode kinetics can be described by the Butler-Volmer expression [36]

$$j_m = j_{0,m}\left[\frac{c^s_{1,m}}{\bar{c}_{1,m}}\exp\left(\frac{\alpha F}{RT}\eta^{ct}_m\right) - \frac{c^{\max}_{1,m} - c^s_{1,m}}{c^{\max}_{1,m} - \bar{c}_{1,m}}\ \frac{c_2}{\bar{c}_2}\ exp\left(-\frac{(1-\alpha)F}{RT}\eta^{ct}_m\right)\right],$$
$$m = \{n, p\} \tag{5}$$

where $j_{0,m}$ is the exchange flux density of Na-ions across the electrode surface of the electrode particles [mol m^{-2} s^{-1}], α is the anodic transfer coefficient [-], R the gas constant [8.314J mol^{-1} K^{-1}], T the temperature [K], F Faraday's constant 95,485 [C mol^{-1}], η^{ct}_m the charge transfer overpotential, $c^s_{1,m}$, $c^{max}_{1,m}$ and $\bar{c}_{1,m}$ the surface, maximum and average concentrations of intercalated Na^+ in the

electrode particles, respectively [mol m^{-3}], and c_2 and $\bar{c}_2$ are the instantaneous and average concentrations of Na^+ in the electrolyte phase, respectively, [mol m^{-3}]. $j_{0,m}$ can be expressed as

$$j_{0,m} = F\ k_m\ \left(c_{1,m}^{max} - \bar{c}_{1,m}\right)^{\alpha_a}\ (\bar{c}_2)^{\alpha_a}\ (\bar{c}_{1,m})^{\alpha_c},\ \ m = \{n, p\} \tag{6}$$

where k_m is the charge transfer rate constant [m$^{2.5}$ mol$^{-1.5}$s^{-1}]. The charge transfer overpotential, η_m^{ct} can then be expressed as

$$\eta_m^{ct} = \varphi_{1,m} - \varphi_{2,m} - U_m\left(c_{1,m}^s, T\right),\ \ m = \{n, p\} \tag{7}$$

where $\varphi_{1,m}$, $\varphi_{2,m}$ and U_m are the electrode, electrolyte, and equilibrium potentials (EMF), respectively [V]. The EMF potentials for both the HC and NVPF electrodes were experimentally determined as described in an accompanying publication [27].

3.3. Current distribution

Throughout the separator and porous electrode regions, the current is distributed between the electronic current density ($i_{1,m}$) and the ionic current density in the solid and electrolyte phases ($i_{2,m}$). Both $i_{1,m}$ and $i_{2,m}$ are related to the total applied current density $i_{app} = I_{app}/A_{cc}$ as

$$i_{app} = i_{1,m} + i_{2,m},\ \ \forall m. \tag{8}$$

Eq. (8) is a form of charge conservation law.

$i_{1,s} = 0$ in the separator region where $m = s$

$$i_{app} = i_{2,s}. \tag{9}$$

At the current collector boundaries of the porous electrodes

$$i_{2,n}|_{x=0} = i_{2,p}|_{x=L} = 0. \tag{10}$$

The boundary condition in Eq. (10) specifies that only an electronic current is present at the current collectors. Applying Eq. (8), therefore, results in

$$i_{app} = i_{1,n}|_{x=0} = \ i_{1,p}|_{x=L}. \tag{11}$$

In the porous electrodes where $m = \{n, p\}$), $i_{1,\mathrm{m}}$ can be modeled by Ohm's law

$$i_{1,\mathrm{m}} = -\sigma_m^{eff}\frac{\partial \varphi_{1,\mathrm{m}}}{\partial x},\ \ m = \{n, p\} \tag{12}$$

where σ_m^{eff} is the effective electronic conductivity in the porous electrode [Ω^{-1} m^{-1}]. In addition, the derivative of $i_{2,m}$ is proportional to j_m in Eq. (5). This relation is expressed as

$$\frac{\partial i_{2,m}}{\partial x} = a_m F j_m,\ \ m = \{n, p\} \tag{13}$$

where a_m is the electrode active surface area, volume ratio [m^{-1}]. a_m is calculated from the particle radius and the electrode porosity as

$$a_m = \frac{3\left(1 - \varepsilon_m^{el} - \varepsilon_m^{filler}\right)}{R_m},\ \ m = \{n, p\} \tag{14}$$

where ε_m^{el} and ε_m^{filler} are the electrolyte and additive filler volume fractions, respectively. ε_m^{filler} includes the binder and conductive filler additives.

3.4. Electrolyte potential and mass distribution

The dilute solution theory governs the electrolyte potential distribution in the liquid electrolytes. This theory is based on the Nernst-Planck equation, a classical description of the transport of charged ionic species in electrolyte media [37]. The dilute solution theory essentially considers binary interactions between ionic species and the solvent and neglects ion-ion pairing effects [38].

Because the $NaPF_6$ $EC_{0.5}$: $PC_{0.5}$ (w/w) electrolyte does not show extensive ion-pairing effects in the concentration range of 0 to 2 mol kg^{-1} as earlier determined [39], electrolyte potential can thus be modeled by the expression [40].

$$i_{2,m} = -\kappa_m^{\mathrm{eff}}\ \frac{\partial \varphi_{2,\mathrm{m}}}{\partial x} + \frac{\kappa_m^{\mathrm{eff}} RT}{F}(1 - 2t_+)\cdot \nabla \ln c_2,\ \ \forall m \tag{15}$$

where κ_m^{eff} is effective ionic conductivity in the electrolyte in cell domain m [Ω^{-1} m^{-1}], and t_+ is the cationic transference number [-], defined as the fraction of $i_{2,s}$ due to cationic migration in the absence of diffusion and convection forces. The definition of $\varphi_{2,\mathrm{m}}$ results in the multiplier $(1 - 2t_+)$, which is different from the multiplier $2(1 - t_+)$ used in other works [41].

A Dirichlet boundary condition is thus defined for the electrolyte potential at the anode

$$\varphi_{2,n}|_{x=0} = 0 \tag{16}$$

Eq. (16) sets $\varphi_{2,n}$ as the reference potential for all potential difference measurements. Another option is to set $\varphi_{1,n}|_{x=0} = 0$, which is equivalent to grounding the anode. In either case, the position and choice of the reference potential do not affect the overpotentials and the overall cell voltage [12]. However, the convenience of the boundary condition in Eq. (16) is that electrode potentials $\varphi_{1,n}$ and $\varphi_{1,p}$ have values similar to those obtained experimentally using a reference electrode of the first kind. This property makes the model validation based on individual electrode potentials using the Na-RE straightforward.

The electrolyte concentration mass balance in the porous electrode region is expressed as

$$\frac{\partial c_2}{\partial t} = \frac{\partial}{\partial x}\left(D_{2,m}^{eff}\ \frac{\partial c_2}{\partial x}\right) + (1 - t_+)a_m j_m,\ \ \forall t, m = \{n, p\} \tag{17}$$

and in the separator region as

$$\frac{\partial c_2}{\partial t} = \frac{\partial}{\partial x}\left(D_{2,s}^{eff}\ \frac{\partial c_2}{\partial x}\right),\ \ \forall t \tag{18}$$

where $D_{2,m}^{eff}$ is the effective diffusion coefficient in the electrolyte based on thermodynamic driving forces [m^{2}s^{-1}]. $D_{2,m}^{eff}$ is a function of c_2, the electrolyte concentration and therefore should not be factored out of the brackets. For a binary electrolyte, $D_{2,m}^{eff}$ is equal to the harmonic mean of the anionic and cationic diffusion coefficients [40].

Two symmetrical Neumann boundary conditions are needed to resolve the concentration profile. These are expressed at the negative electrode/current collector boundary ($x = 0$) and at the positive electrode/current collector boundary ($x = L$) as

$$\frac{\partial c_2}{\partial x}|_{x=0} = 0, \tag{19}$$

$$\frac{\partial c_2}{\partial x}|_{x=L} = 0. \tag{20}$$

Boundary conditions Eqs. (19) and 20 state that there is no flux of ionic species at the current collector/electrode interface. These are identical in the case of a full cell battery with two porous electrodes.

In addition, an initial condition is needed for c_2, which is defined as

$$c_2(x, t = 0) = \ c_2^0, \tag{21}$$

where c_2^0 is the initial concentration at rest/equilibrium, equal to 1 kmol m^{-3}. Based on experimental conductivity studies, the conductivity of $NaPF_6$ in $EC_{0.5}$: $PC_{0.5}$ (w/w) electrolyte is also highest around this concentration [39].

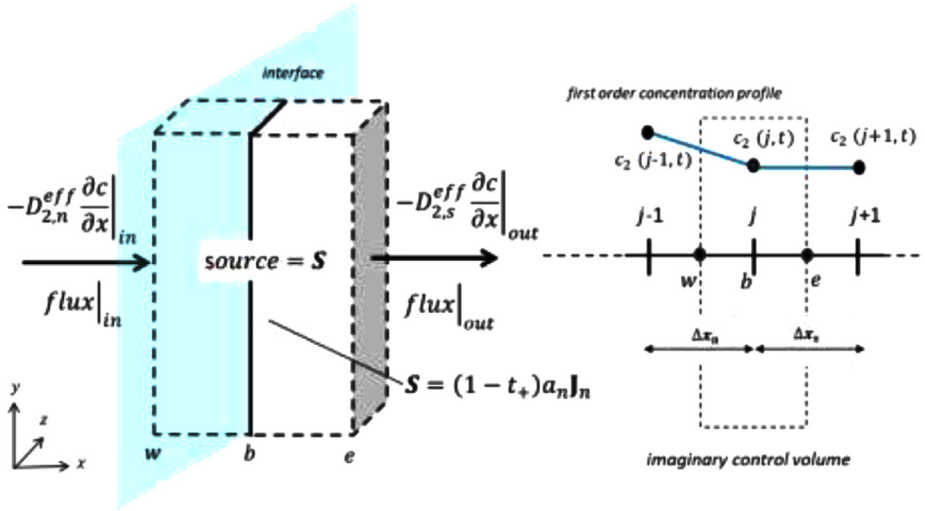

Fig. 2. Control volume method showing the microscopic mass balance and interface discretization for the boundary of the separator and porous electrode.

3.5. Relation between bulk transport properties and porous electrode properties

Bulk properties such as the diffusion coefficients and the electrode conductivity need to be related to the volume fraction of the bulk material in the porous electrode. The Bruggeman correlation [42] is herein used to define the effective electrolyte transport properties of conductivity and diffusion coefficient

$$\kappa_m^{\text{eff}} = (\varepsilon_m^{el})^{1.5} \cdot \kappa, \ \forall m, \tag{22}$$

$$D_{2,m}^{\text{eff}} = (\varepsilon_m^{el})^{1.5} \cdot D_2, \ \forall m \tag{23}$$

where κ and D_2 represent the bulk electrolyte conductivity and diffusion coefficient, separately determined by conductivity experiments and the advanced electrolyte model (AEM) version 2.19.1 [39]. The AEM is a statistical-mechanics-based simulation model for determining electrolyte properties [43–45].

A brief discussion on the Bruggeman exponent value of 1.5 in Eqs. (22) and 23 is necessary. This exponent includes a hidden factor of 1, which correlates the bulk electrolyte concentration to the porous media concentration

$$c_{2,m} = \varepsilon_m^{el} \cdot c_2, \tag{24}$$

where $c_{2,m}$ is the electrolyte concentration, which includes the volume of the solid phases in porous media [mol m^{-3}]. It is equally valid to use the Bruggeman exponent of 0.5, in which case, the correlated $c_{2,m}$ is used in the model equations. The advantage, however, of using the uncorrelated concentration c_2 is that electrolyte concentrations in different cell domains can be treated as continuous functions.

The Bruggeman correlation was nevertheless not used for σ_m^{eff} since there was no prior knowledge of the bulk electrode conductivity and the electrode porosity was not fixed. Therefore, the optimization of the electrode conductivity was performed for the effective property without including a correlation.

3.6. Modeling interfaces

The first-order and second-order PDEs in the electrolyte were discretized by a finite difference method (FDM). Because of porosity differences in the battery domains, the transport properties can change across the interface. Thus the FDM mass balance may be inaccurate across the interface. To overcome this, some authors have proposed an effective interfacial diffusion coefficient [12]. In this work, however, a control volume method (CVM) was used to discretize the interfacial boundary of the separator and porous electrode. Detailed descriptions of the CVM have been published [46]. For the interested reader, Botte *et al.* [47,48] compared the FDM and the CVM in battery modeling applications. In general, the CVM results in perfect mass conservation across the interface. To obtain the concentration at the interface node, an imaginary control volume is defined across the interface node, and fluxes across the faces of the imaginary volume are calculated, assuming a linear concentration profile. Fig. 2 illustrates the elements of the CVM herein used to derive the interfacial concentration.

The interfacial concentration at the negative electrode/separator interface can therefore be determined as

$$\frac{\partial c}{\partial t}|_b = \frac{1}{(\varepsilon_n \Delta x_n + \varepsilon_s \Delta x_s)} \times \left[2D_{2,s}^{\text{eff}} \frac{\partial c}{\partial x}\ |_e - 2D_{2,n}^{\text{eff}} \frac{\partial c}{\partial x}\ |_w + a_n j_n \Delta x_n (1 - t_+) \right], \tag{25}$$

where Δx_n and Δx_s are the node spacings in the negative electrode and separator [m], respectively, while b, e, and w are representing the interface, the outermost east boundary, and the west outer boundary of the imaginary control volume, respectively. A similar mass balance in a control volume expression can be derived at the positive electrode/separator interface.

3.7. Battery voltage

Finally, a Dirichlet boundary condition for the electrode potential on each electrode must be considered [49]. Suppose that the electrode potentials at the left boundary of each porous electrode ($\varphi_{1,n}|_{x=0}$ and $\varphi_{1,p}|_{x=\delta_n+\delta_s}$) are set to some arbitrary values. These values influence the ionic current densities at the opposing electrode end at $i_{1,n}|_{x=\delta_n}$ and $i_{2,p}|_{x=L}$, respectively. To ascertain if the imposed boundary conditions are correct, Eq. (9) and the boundary conditions of Eqs. (10) and 11 must be satisfied. The functions to be solved at the negative electrode and the positive electrode can therefore be expressed by

$$I_{1,n}(\varphi_{1,n}|_{x=0})/A_{\text{cc}} = i_{1,n}|_{x=\delta_n} = 0 \tag{26}$$

and

$$I_{2,p}\left(\varphi_{1,p}|_{x=\delta_n+\delta_s}\right)/A_{\text{cc}} = i_{2,p}|_{x=L} = 0, \tag{27}$$

where $I_{1,n}$ represents electronic current at the interface between the anode and separator, while $I_{2,p}$ represent the ionic current at

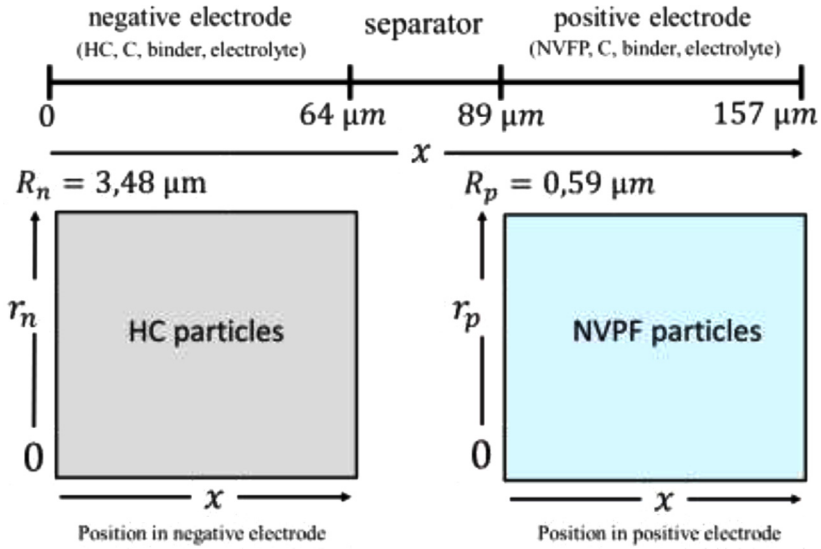

Fig. 3. P2D model setup and dimensions of the studied HC//NVPF SIB.

the interface with the cathode current collector. These currents are considered as generated by coupled PDEs for the negative and positive electrodes, respectively.

Eqs. (26) and 27 can be solved by various iterative root-finding methods, in which an approximate value of the electrode potential is supplied as an initial guess. In the literature, such a method is also called 'shooting' [50,51]. In this model, a combination of the dichotomy method and the secant method is applied to optimize the solution convergence [52]. Because the system of equations in porous battery electrodes is nonlinear, it is possible to obtain intermediate solutions of extreme magnitude for minor deviations in the initial guess. A robust root finding method is therefore needed in the first iterations. To our knowledge, the dichotomy method is the only method capable of finding the root in cases where solutions on the right-hand side of the equation can have infinite values. The dichotomy method uses two guess values of the electrode potential, an overestimate and an underestimate, and then reduces the estimated range until the solution is found within the error tolerance. In this case, the tolerance is set at 0.01% of i_{app}. However, the dichotomy method requires many iterations and is therefore slow to converge to the root. For faster root finding, the solution method switches to the secant method after 5 iterations of the dichotomy method, when the right-hand side value is finite.

Once the solution is found within the error tolerance, the full cell battery voltage can then be determined by

$$V_{bat} = \varphi_{1,p}|_{x=L} - \varphi_{1,n}|_{x=0} - (R_{contact,n} + R_{contact,p})\, i_{app} \quad (28)$$

where $R_{contact,n}$ and $R_{contact,p}$ [Ω m^2] are the negative and positive electrode current collector/porous electrode contact specific resistances, respectively. The importance of the contact resistance is revealed at high currents [13,53]. In this work, the contact resistances of individual electrodes were calculated from the Na-RE measurements [27].

It is worth highlighting that the validation of the model vs. experimental data is done based on the individual electrode potentials and not the full cell voltage, V_{bat}. This scheme is applied because, from Eq. (28), it is possible to have wrong values of both $\varphi_{1,p}$ and $\varphi_{1,n}$ and yet still manage to have a correct V_{bat}. The Na-RE electrode deconvolutes the individual electrode potentials from V_{bat} and thereby allows model validation on two separate electrodes.

The electrode potentials used for validation of the model vs. experimental data can thus be expressed as

$$\mathrm{V_p} = \varphi_{1,p}|_{x=L} - A_{cc}\, R_{contact,p}\, i_{app} \quad (29)$$

and

$$\mathrm{V_n} = \varphi_{1,n}|_{x=0} + A_{cc}\, R_{contact,n}\, i_{app}, \quad (30)$$

where V_p and V_n [V] are the positive and negative electrode potentials, respectively.

4. Parameter identification and optimization

For the developed model to provide physically meaningful results, the model parameters should be inferred from an extensive experimental data set. Because of the minimal assumptions in P2D models, experimentally derived parameters should ideally result in a fitting model. However, due to the disparity in the definitions of key parameters, such as the diffusion coefficients and transference number between experimental and modeling techniques, this is seldom the case. Another challenge is that experimentally derived parameters are technique-dependent. There is, therefore, a great need to bridge the gap between model and experimental parameters. Nevertheless, experimental parameters are an ideal starting point and provide insight into the order of magnitude of the model parameters.

In this work, the geometric parameters of the SIBs were determined from experiments and used without modification [27]. These include the thicknesses of the electrodes and separator as well as the particle radii of the positive and negative electrodes. Fig. 3 shows the cell dimensions of the HC//HVPF SIB, concluded from the experiments.

The negative electrode is therefore defined between $0 \leq x \leq 64$ µm, the separator in the $64 \leq x \leq 89$ µm region, while the negative electrode is defined in the $89 \leq x \leq 157$ µm region. The HC and NVPF electrode particles are separately modeled in a homogenous P2D domain, in which the r_m- and x- axis represent the particle radii and particle positions in the porous electrode, respectively. Having fixed cell dimensions allows the mesh of the cell components to be defined in the model. Changes in cell dimensions during optimization require a new mesh to be defined, which may inadvertently affect parameters with length scale, such as the conductivity and diffusion coefficients. This problem can also lead to numerical instabilities and inconsistent model results. It is therefore advised to maintain constant cell dimensions unless experimental evidence proves otherwise.

The EMF of the NVPF and HC electrodes were also determined from experimental data based on the slow discharge rate

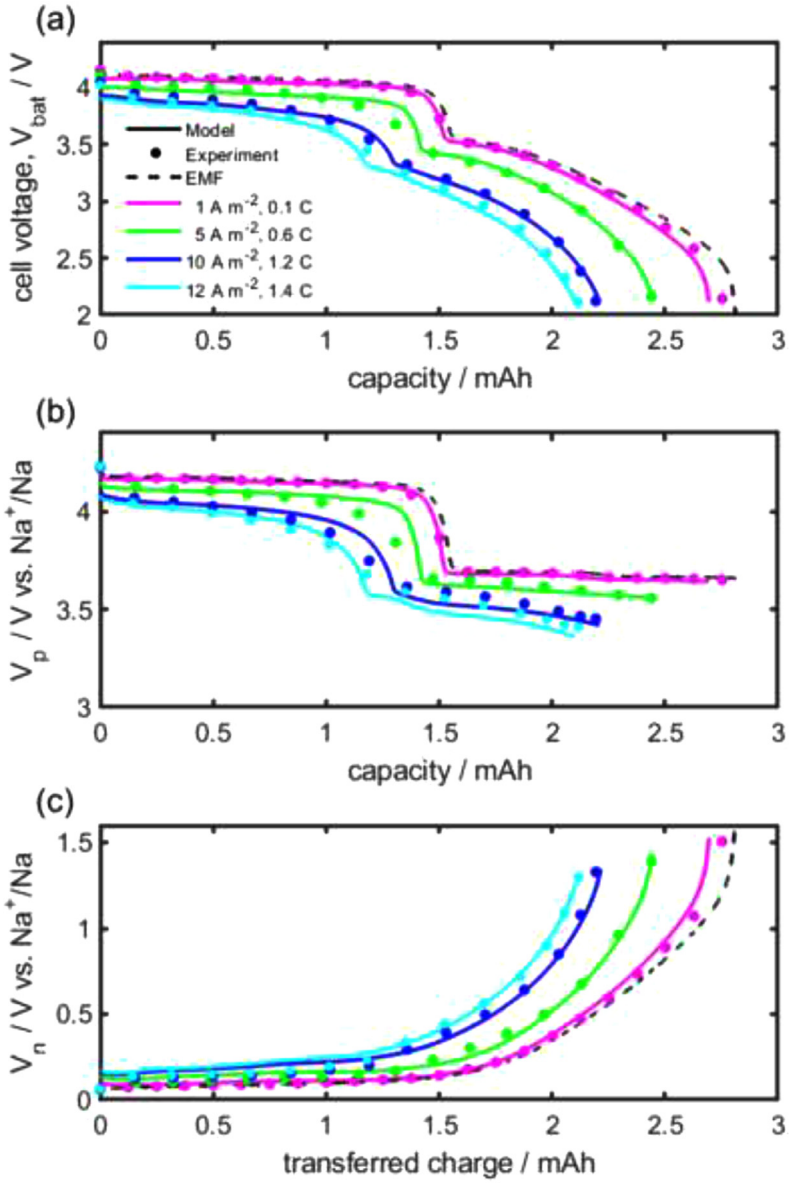

Fig. 4. Simulated (solid lines) and experimental (symbols) results of an optimized P2D model for an HC//NVPF SIB. Battery voltage (a) and potential of the positive electrode (b) and negative electrode vs. Na-RE (c). Dashed lines show the corresponding EMF curves.

experiments [27]. The particle-phase diffusion coefficients, $D_{1,m}$ and kinetic rate constants, k_m were determined from a combination of experimental GITT and P2D modeling approach (P2D GITT model) [34]. A half-cell P2D GITT model was used in combination with half-cell GITT experimental data to determine the HC and NVPF transport parameters at different electrode SOC. As a result, concentration-dependent $D_{1,n}(c_{1,n})$, $D_{1,p}(c_{1,p})$, $k_n(c_{1,n})$ and $k_p(c_{1,p})$ were thus obtained. On the other hand, electrolyte properties of $D_2(c_2)$, $\kappa(c_2)$ and t_+ were determined from the AEM modeling and experiments [39].

Appendix A lists the parameters used in the model. Constant value parameters are listed in Table A1, while concentration-dependent parameters for the HC negative electrode, NVPF positive electrode and $NaPF_6$ $EC_{0.5}$: $PC_{0.5}$ (w/w) electrolyte are shown in Figs. A1, A2, and A3, respectively. These figures also show a comparison between the experimental and model optimized parameters.

For optimizing the unknown model parameters, the root-mean-square error between the model and the experimental results was defined as the objective function. The MATLAB genetic algorithm (GA) was used to obtain the error minimum for multiple discharge curves at different rates [54]. The GA is necessary due to the non-linearity of the P2D model equations and parameter identification complexity. Because of the availability of two experimentally determined electrode potentials for each discharge curve, a two-step optimization procedure was therefore followed, in which parameters for the positive electrode were optimized in the first step, separate from the parameters of the negative electrode, which were then optimized in the second step. The concentration-dependent parameters were optimized by means of a scaling factor. This strategy resulted in improved optimization results at high rates.

5. Results and discussion

Fig. 4 shows the measured (symbols) and simulated (solid lines) SIB discharge voltage profiles as a function of the transferred charge during discharge. The model results are obtained using a single set of optimized parameters for all discharge rates. Discharge

current densities of 1, 5, 10, and 12 A m^2 were applied, corresponding to 0.1, 0.6, 1.2, and 1.4 C-rate, respectively.

Fig. 4a shows the measured and simulated voltage profiles of an HC//NVPF, full cell SIB. The fully-charged cell voltage starts at 4.2 V and terminates at the cutoff voltage of 2 V. Note that the practically recommended cutoff voltage is 2.5 V [55]. As the current increases, the battery voltage and the maximum transferred charge decrease. This is because of an increase in mass transport and charge transfer overpotentials at higher currents. An accurate physics-based model is, therefore, the only way to account for the various kinetic and mass transport effects at different rates.

Fig. 4b and c shows the measured and simulated voltage profiles of the NVPF positive electrode (V_p *vs.* Na-RE) and the HC negative electrode (V_n *vs.* Na-RE), respectively. At the different discharge rates, V_p varies between $4.3 - 3.4$ V *vs.* Na-RE while V_n varies between 0.1–1.5 V *vs.* Na-RE. Therefore, based on the potential range and the current dependence of the voltage profiles, both electrodes contribute significantly to the overpotential losses in the full cell and consequently to the capacity losses at high currents. In both cases, however, the P2D model is in good agreement with the experimental voltage profiles of V_p and V_n *vs.* Na-RE.

Table 1 shows the percentage error in V_{bat} and the mean absolute errors in V_{bat}, V_p and V_n at different rates. The largest percentage error in V_{bat} is 1.47%, corresponding to 48.1 mV in absolute error terms. Therefore, the model results match the experimental full cell voltage and the individual electrode potentials at different discharge rates.

Table 1
Simulation errors obtained at different (dis)charging rates.

[A m^2]	V_{bat} error [%]	Mean absolute voltage error [mV]		
		V_{bat}	V_p	V_n
1	0.70	19.9	8.6	12.4
5	0.96	34.6	33.5	27.7
10	0.95	32.2	37.6	35.2
12	1.47	48.1	37.8	32.6

The accurate P2D model herein presented goes beyond the current density and terminal voltage data by providing additional information on internal battery states. In the subsequent figures, the Na^+ electrolyte concentration, the Na^+ concentration in the active particles, and the ionic current distribution are compared for the applied current of 1 and 12 A m^{-2}, to investigate how different discharge rates influence the battery performance.

Fig. 5a and b show 3D simulation results of the electrolyte concentration, $c_2(x,t)$ at 1 A m^{-2} and 12 A m^{-2} discharge rates, respectively. Here, $c_2(x,t)$ is shown at different cell positions, x and discharge time, t. In the negative electrode region ($0 \leq x \leq 64$ µm),

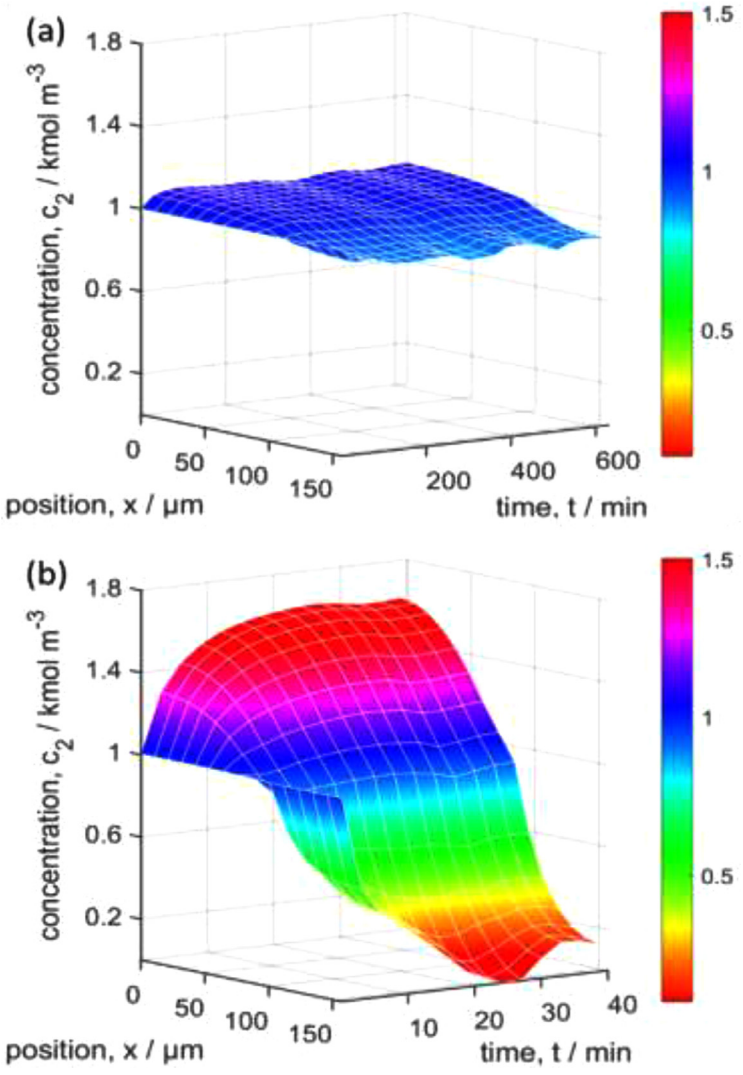

Fig. 5. Evolution of the electrolyte concentration (c_2) profiles as a function of position (x) and discharge time (t) upon discharging at 1 (a) and 12 A m^{-2} (b).

c_2 increases as a function of time due to Na^+ deintercalation in the HC negative electrode, while in the positive electrode region ($89 \leq x \leq 157$ µm), c_2 decreases due to Na^+ intercalation in NVPF. This ionic transport in the electrolyte is driven by migration and diffusion mechanisms, as expressed in Eq. (15). Note that due to electroneutrality condition, at any given time, the average of c_2 remains constant and equal to the equilibrium and initial concentration of 1 kmol m^{-3}.

Although the results in Fig. 5a do not appreciably deviate from1 kmol m^{-3}, these slow-discharge rate profiles, however, show dynamic waves compared to the fast-discharge rate profiles shown in Fig. 5b (see **Fig. S1** in the Supplementary Information at higher magnification). On the other hand, the results in Fig. 5b reveal a severe depletion of Na^+ ions in the positive electrode during fast-discharge. This depletion is exceptionally well visible near the positive current collector boundary ($x = 157$ μm), where c_2 attains a minimum of only 3.7 mol m^{-3} after about 25 min.

The effect of a low c_2 is a sharp increase in η_p^{ct} for a given interfacial flux, j_p (See Eq. (5) for the relationship between j_p, c_2 and η_p^{ct}). An increase in η_p^{ct} results in a reduction in the positive electrode potential and amounts to significant energy losses in the full SIB (see **Fig. S2** for a comparison of profiles of c_2, η_p^{ct} and j_p in the positive electrode during 12 A m^{-2} discharge). This situation can be mitigated by optimizing the electrolyte conductivity, electrode porosity, and coating thickness [56–58]. The optimization objective here is to reduce the electrolyte mass transport limitations, which induce high overpotentials at high current densities.

Fig. 6 shows 1D plots of the simulated results of the intercalated concentration of Na^+ ions, $c_{1,m}$ in the negative and positive electrode active particles. Note that profiles of $c_{1,m}(x, r_m, t)$ develop along the dimension of the particle radius, r_m and positions along the porous electrode coating thickness, x. In order analyze the profiles along x only, it is therefore necessary to plot the average and surface concentrations, $\bar{c}_{1,m}(x,t)$ and $c^s_{1,m}(x,t)$, respectively, at specific times. The results are shown at discharge times, defined as 20, 40, 60, and 80% of the maximum discharge time ($t_{\max}$), where $t_{\max} = 10.92$ h and 41.39 min. for the 1 and 12 A m^{-2} discharge rates, respectively. The $\bar{c}_{1,m}$ plots are shown in dashed lines, while the $c^s_{1,m}$ plots are shown in solid lines. During discharge, the negative electrode concentrations, $\bar{c}_{1,n}$ and $c^s_{1,n}$ decrease (Fig. 6a and c), while the positive electrode concentrations, $\bar{c}_{1,p}$ and $c^s_{1,p}$ increase (Fig. 6b and d).

Fig. 6a and b show the simulated results of the intercalated concentration of Na^+ ions during a 1 A m^{-2} discharge, in the negative and positive electrode active particles, respectively. For the slow-discharge rate operation, $\bar{c}_{1,m}$ and $c^s_{1,m}$ profiles are shown to evolve uniformly along x. In addition, the profiles remain very close at all times. This behavior indicates that slight concentration gradients develop in the electrode active particles during the slow discharge rate. From a modeling perspective, such concentration profiles can be simulated quite accurately using computationally efficient analytical methods [30].

Fig. 6c and d show the simulated results during 12 A m^{-2} discharge in the negative and positive electrodes, respectively. In contrast to the results shown in Fig. 6a and b, the fast-discharge exhibits non-uniform $\bar{c}_{1,m}$ and $c^s_{1,m}$ profiles along x. This is most apparent in the positive electrode (Fig. 6d), where the active particles close to the separator receive 58% higher average concentration at compared to particles at the current collector (compare $\bar{c}_{1,p}$ at $x = 89$ and $x = 157$ μm in the dashed curves of Fig. 6d). These profiles can only be obtained accurately using numerical methods because of the concentration dependence of $D_{1,n}$ and $D_{1,p}$.

An analysis of the difference $c^s_{1,m} - \bar{c}_{1,m}$ is shown in Supplementary Information **Fig. S3** as a function of discharge time. **Fig. S3**a and c show the concentration difference in the negative electrode particles, ($c^s_{1,n} - \bar{c}_{1,n}$) while **Fig. S3**b and d show the difference in the positive electrode particles, ($c^s_{1,p} - \bar{c}_{1,p}$). A small difference indicates negligible concentration gradients in the electrode active particles. Such behavior is desirable because high concentration gradients induce mechanical strain in the particles [59]. At slow discharge rates (**Fig. S3**a and b), $c^s_{1,m} - \bar{c}_{1,m}$ is not large. The maximum differences are about 0.8 and 0.25 kmol m^{-3} in the negative and positive electrodes, respectively. At fast discharge rates, however (**Fig. S3**b and c), $c^s_{1,m} - \bar{c}_{1,m}$ is significantly large. The maximum differences are about 3.5 and 2 kmol m^{-3} in the negative and positive electrodes, respectively. In addition, compared to the negative electrode profile (**Fig. S3**c), the positive electrode profile monotonically increases with time (**Fig. S3**d). This increase indicates diffusion transport limitations in the NVPF particles as a result of the comparatively low $D_{1,p}$ of the material. Such behavior is also consistent with diffusion length calculations, wherein the diffusion times for HC and NVPF were estimated to be 1 and 2 h, respectively [27].

Supplementary Information **Fig. S4** shows profiles of the interfacial flux, j_m at discharge rates of 1 (**Fig. S4**a and b) and 12 A m^{-2} (**Fig. S4**c and d). In order to analyze the distribution of the flux, the profiles are averaged over quarterly intervals of t_{max}. It can be observed that the initial stages (red lines) are characterized by high j_m rates at the electrode/separator boundary. Another observation is that profiles in the negative electrode at 1 and 12 A m^{-2}, **Fig. S4**a and c respectively are nearly identical and scaled versions of each other. This similarity indicates that the distribution of j_m in the negative electrode is not altered by the increase in the discharge rate. In contrast, profiles in the positive electrode (**Fig. S4**b and d) show considerable differences, especially in the intermediate periods $0.25\ t_{max} < t \leq 0.5\ t_{max}$ (blue line) and $0.5\ t_{max} < t \leq 0.75\ t_{max}$ (green line). This indicates that high discharge rates are influencing the distribution of j_m in the positive electrode.

Fig. 7 shows 2D simulation results of the intercalated Na^+ concentration in the negative (Fig. 7a-d) and positive (Fig. 7e-h) electrodes during a 1 A m^{-2} discharge rate. For an illustration of the relationship between 1D and 2D coordinates, refer to Fig. 3. The 2D results in Fig. 7 show in more detail the 1D profiles shown in Fig. 6a and b. The 2D concentrations are, however, expressed as SOC, which is defined for the negative and positive electrodes as

$$SOC_n(r,t) = \frac{c_{1,n}(r,t)}{c_{1,n}^{max}} \tag{31}$$

$$SOC_p(r,t) = 1 - \frac{c_{1,p}(r,t)}{c_{1,p}^{max}} \tag{32}$$

The SOC scale is convenient for a side-by-side comparison of the 2D concentration profiles in two battery electrodes because the SOC is scaled between 0 and 1 or 0 and 100%.

At low discharge rates, the SOC is uniformly distributed within the active particles (along the r_m-axis) and for particles located at different positions in the electrodes (along the x-axis). In addition, toward the end of discharge (Fig. 7d and h, $t = 80\%\ t_{max}$), the SOC is low and uniformly distributed in both electrodes. This behavior signifies that the intercalated Na^+ is optimally utilized and that the maximum extractable capacity is attained. The electrode thickness can also be safely increased without harming the discharge performance of the cell at this discharge rate.

Fig. 8 shows the 2D SOC profiles in particles of the HC (Fig. 8a-d) and NVPF (Fig. 8e-h) electrodes at a discharge rate of 12 A m^{-2}. The results in Fig. 8 further elaborate the 1D profiles shown in Fig. 6c and d. In contrast to the uniform concentration profiles observed in Fig. 7, the fast discharge rate reveals non-uniform SOC distribution in both the x- and r_m-axis.

Fig. 8a-d show the evolution of SOC profiles in the HC negative electrode at the various indicated times. Compared to

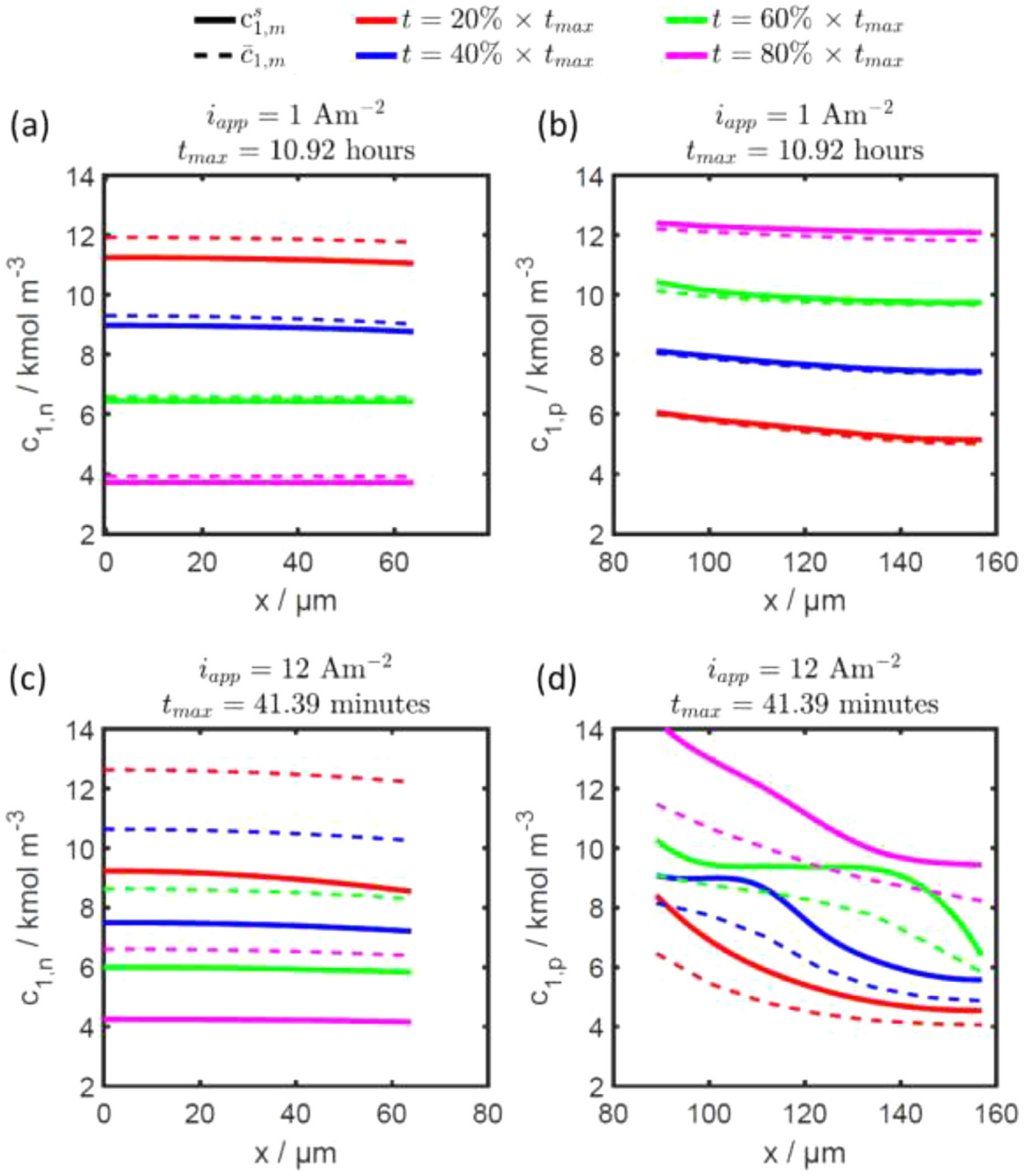

Fig. 6. Simulated intercalated Na^+ concentration at the active particle surface, $c^s_{1,m}$ (solid lines) and the average concentration in the active particles, $\bar{c}_{1,m}$ (dashed lines) in the porous HC negative electrode ($m = n$) (a),(c) and in the NVPF positive electrode ($m = p$) (b),(d) as a function of position (x) and various indicated discharge times related to t_{max} during discharging at 1 (a),(b) and 12 A m^2 (c),(d).

slow-discharge profiles (Fig. 7a-d), the SOC is non-uniformly distributed during the fast-discharge rate. It can also be observed that, for the negative electrode, the differences in SOC mainly develop inside the particles (along the r_n-axis) compared to the electrode thickness (along the x-axis). For example, toward the end of discharge in Fig. 8d, although the SOC at the surface ($r_n = 3.48$ μm) is low, approximately 0.2, it remains high at the center of the HC particles ($r_n = 0$), approximately 0.8. In fact, the changes in SOC at the center of HC particles are insignificant at all times shown. This implies that the HC particles are too large for efficient charge transfer at fast and continuous discharge rates. Nevertheless, because of the high $D_{1,n}$ [27], this SOC at the center of the particles can still be recovered by setting the SIB in relaxation.

Fig. 8e-h shows the evolution of SOC profiles in the NVPF positive electrode along both the x- and r_p-axis at various indicated times. During the fast-discharge rate, and similar to the SOC profiles shown in the negative electrode (Fig. 8a-d), the SOC profiles are also non-uniformly distributed. However, in contrast to the negative electrode profiles in Fig. 8a-d, differences in SOC develop both inside the particles (along the r_p-axis) and along the electrode thickness (along the x-axis). In addition, there are significant changes in the SOC at the center of the particles ($r_p = 0$) during discharge. The small NVPF particle radius (0.59 μm) compared to

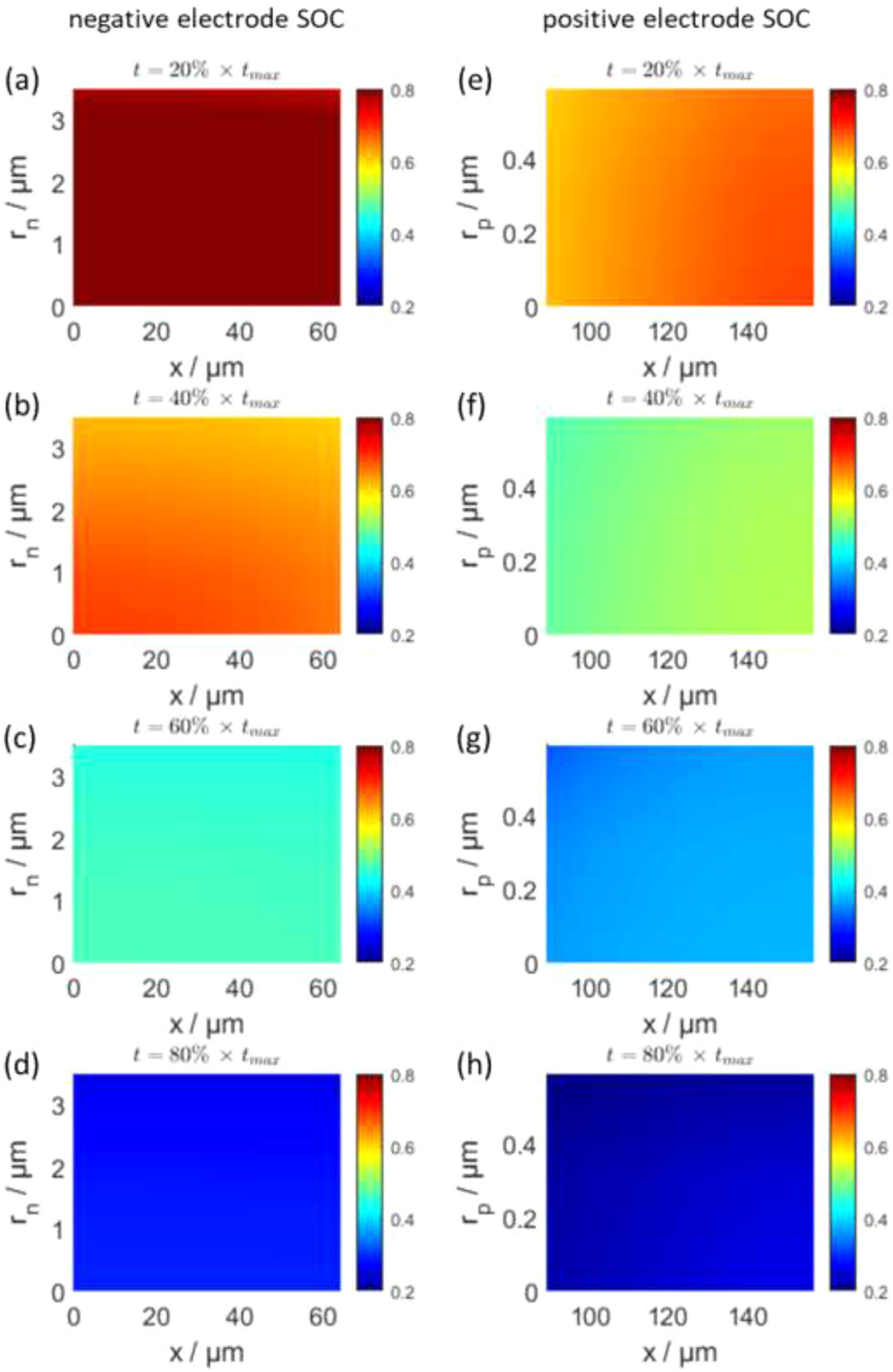

Fig. 7. SOC profiles along active particle radii, r_m and active particles position, x in the negative electrode ($m = n$) (a) to (d), and in the positive electrode ($m = p$) (e) to (h). Profiles are obtained at 1 A m^{-2} for which t_{max} = 10.92 h.

the HC particle radius (3.48 μm), therefore, results in more efficient charge insertion in the positive electrode.

The SOC profiles along the x-axis in Fig. 8e-h also mirror the electrolyte concentration profiles shown in Fig. 5b. The low electrolyte concentration close to the positive electrode current collector ($x = 157$ µm) means the NVPF particles in this region are underutilized compared to the active material close to the separator. Such a variation of SOC along the electrode thickness is detrimental to the battery's performance because intercalated Na^+ cannot diffuse between adjacent particles. This issue is analogous to a cell

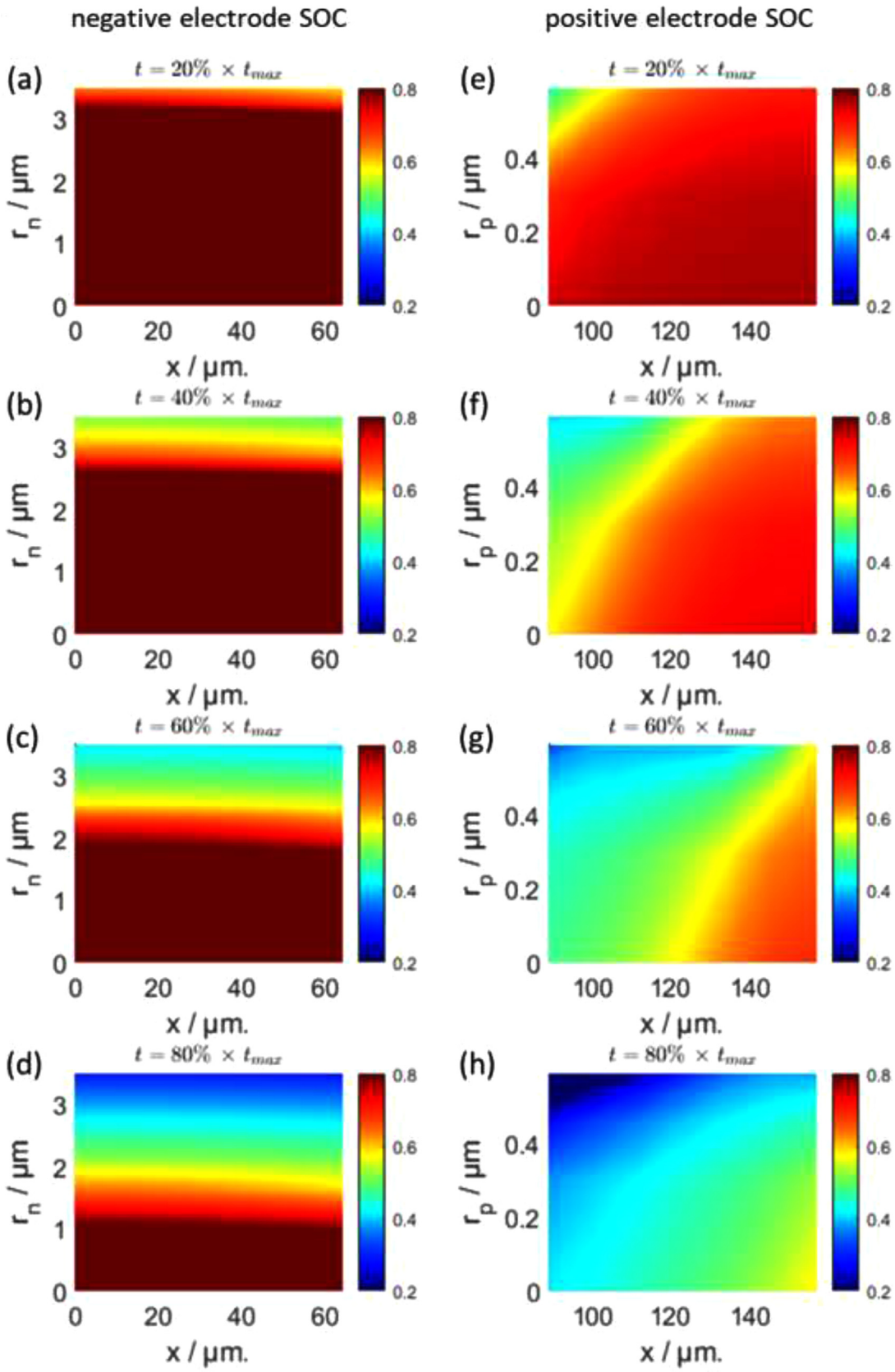

Fig. 8. SOC profiles along active particle radii, r_m and active particles position, x in the negative electrode ($m = n$) (a) to (d), and in the positive electrode ($m = p$) (e) to (h). Profiles are obtained at 12 A m^{-2} for which t_{max} = 41.39 min.

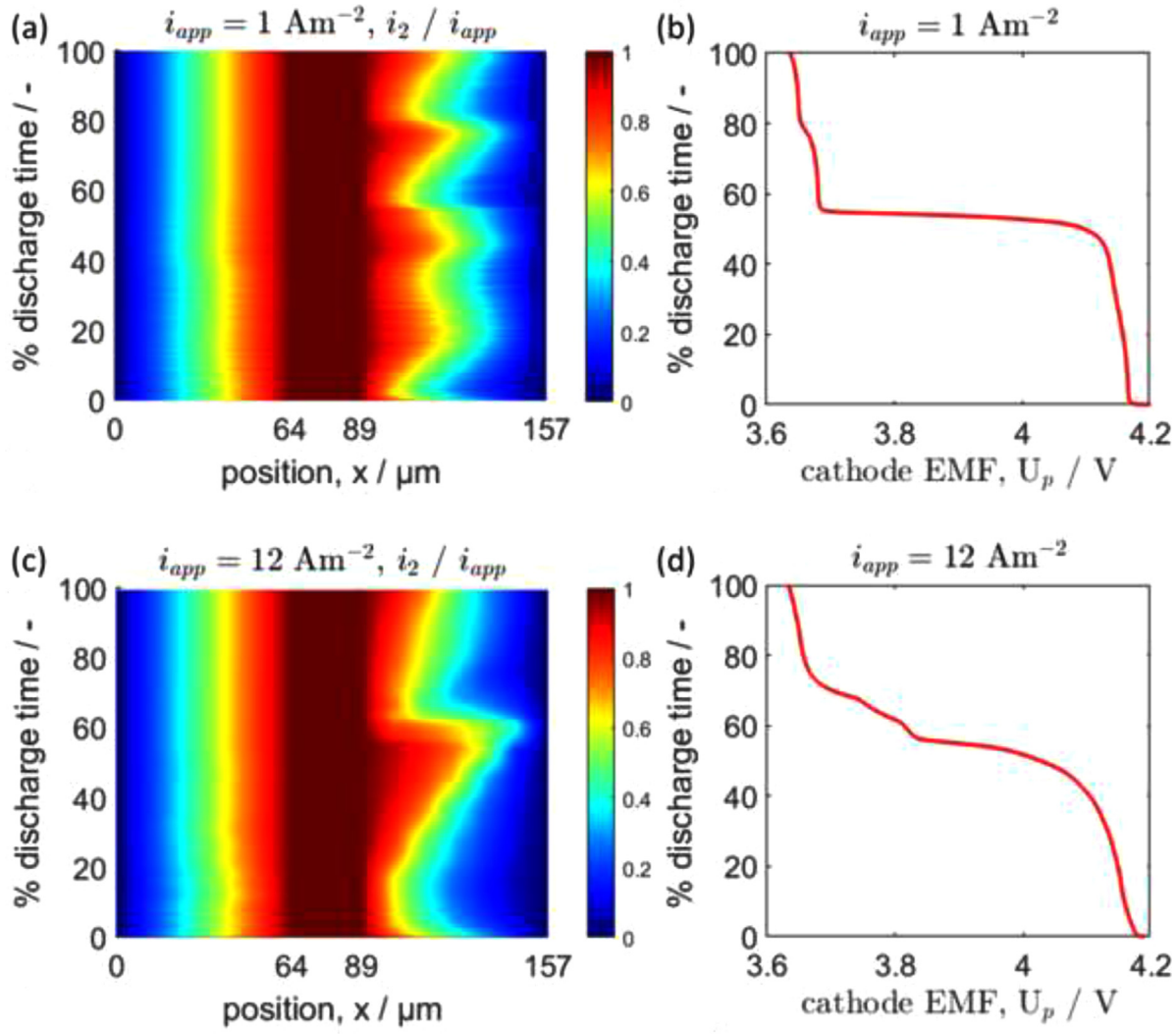

Fig. 9. Profiles of the electrolyte current density, i_2 at different positions, x and% discharge time. The i_2 profiles are normalized with respect to the applied current i_{app} and compared with the voltage profile of the NVPF cathode. (a) and (b) i_2/i_{app} and NVPF voltage profiles at 1 A m^{-2} respectively. (c) and (d) i_2/i_{app} and NVPF voltage profiles at 12 A m^{-2} respectively. The stair-case voltage profile of the NVPF electrode results in the nonlinear i_2 profile in the cathode.

balancing problem in a battery module, although we are talking here of imbalances occurring along the electrode thickness. Consequently, increasing the electrode coating thickness without improving the electrolyte mass transport will result in greater imbalances and a huge penalty in terms of capacity loss for the HC//NVPF SIB.

Fig. 9 shows the simulated results of ionic current density, $\boldsymbol{i}_2$ in 2D color plots and the EMF of the positive electrode, $\boldsymbol{U_p}$ in 1D plots as a function of the discharge time $\boldsymbol{t}$ (expressed as a percentage of $\boldsymbol{t_{max}}$). The results of $\boldsymbol{i}_2$ are also shown as a function of position $\boldsymbol{x}$, and they are normalized with respect to $\boldsymbol{i_{app}}$, as indicated in the color code at the right-hand side of Fig. 9a and c. Here, $\boldsymbol{i}_2$ represents the flux of $\mathbf{Na}^+$ due to migration and diffusion in the electrolyte phase (see Eq. (15)). The results show that $\boldsymbol{i}_2 = 0$ at the current collector ($x = 0$ and $x = 157$ μm) and $\boldsymbol{i}_2 = \boldsymbol{i_{app}}$ at the separator ($64 \leq \boldsymbol{x} \leq 89$ μm). This is in accord with the boundary conditions and thus validates the solution method in Eqs. (26) and 27.

Fig. 9a and b show i_2 profiles and the corresponding U_p during 1 Am^{-2} discharge rate, respectively, while Fig. 9c and d show i_2 and U_p during 12 Am^{-2} discharge rate, respectively. It can be observed that i_2 profiles are linear in the negative electrode and nonlinear in the positive electrode, irrespective of the discharge rate. In addition, based on the side-by-side comparison of i_2 and U_p, it can be observed that the nonlinear i_2 profiles in the positive electrode align with the step changes in the corresponding EMF of the NVPF. Therefore, the 'staircase' NVPF EMF results in nonlinear i_2 in the positive electrode. Results in Fig. 9 demonstrate that even in the cases of a slow discharge rate, the profiles of i_2 can be quite dynamic, which can pose a challenge for reduced-order models to be accurate in the case of SIBs.

Fig. 10 shows a comparison of the experimental and simulation results of the HC//NVPF SIB in a Ragone plot. This figure compares the energy and power characteristics of the SIB. The simulation results are very close to the experimental results up to the 1-hour discharging rate. At higher rates, deviations appear, which can be explained by phase changes in the NVPF active material, which are not included in the solid-solution model. To improve accuracy at higher rates, a multi-phase diffusion mechanism is therefore needed to model phase transformations in the NVPF active material [60,61]. Nevertheless, the improvements brought by concentration-dependent $D_{1,m}$ and k_m result in a close match between the experiment and model predictions while maintaining a single set of parameters for all rates.

Often, in battery design, increasing the battery's energy density results in decreased power density. As a result, optimizing battery performance is nontrivial. However, the model herein presented can be used to determine design parameters, such as electrode

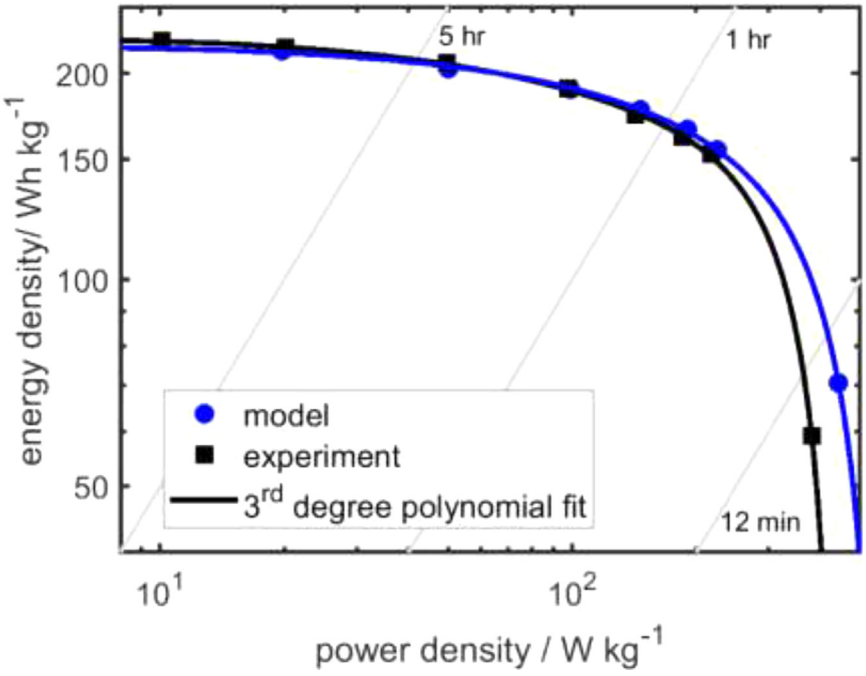

Fig. 10. Ragone plot of the HC//NVPF SIB showing the simulation (blue) and experimental (black) results.

thickness and porosity, based on the accuracy shown in the Ragone plot. At the same time, battery manufacturing costs should not be neglected, which can also be part of a multi-objective optimization procedure [62]. For example, increasing the coating thickness reduces the cost but simultaneously reduces the battery's power [63,64]. These factors can be combined and investigated using this SIB P2D model as a strategy and tool to avoid the often-expensive experimental trial and error methods.

6. Conclusions

A pseudo-two-dimensional (P2D) model is herein shown to model the voltage of a sodium-ion battery (SIB) composed of $Na_3V_2(PO_4)_2F_3$ (NVPF) and hard carbon (HC) as positive and negative electrodes, respectively. The HC//NVPF SIB model uses a coupled set of partial differential equations (PDEs) for the current and concentration profiles. An iterative root finding method is applied to determine the solution of the coupled system of PDEs. The model parameters are obtained by a genetic algorithm, a gradient-free optimization method. The negative and positive electrode parameters are optimized separately to reduce the number of simultaneously optimized parameters and improve accuracy. It is shown that the model is least accurate by 1.47% at a 1.4 C-rate using a constant set of parameters.

The developed P2D model can be rapidly parametrized using experimentally derived data. The voltage profiles for individual electrodes were obtained at different C-rates using a reference electrode and were used to determine parameters for each electrode. Using the validated P2D SIB model, more information concerning internal cell dynamics was obtained, which allowed an analysis of the limiting factors. It is shown that the high C-rate performance of the HC//NVPF SIB is limited by the poor mass transport in the HC and NVPF electrodes and in the electrolyte. Mass transport in HC electrodes can be improved by reducing the particle sizes. In contrast, the NVPF particles suffer from a low diffusion coefficient.

The model herein shown can be used as a design tool to improve the performances of SIBs, starting with the limiting factors already identified. Future works will thus focus on multi-objective optimization of the cell design, including electrode thickness and material costs as additional design considerations. In addition, model accuracy can be improved by including temperature effects in large format cells and multi-phase intercalation dynamics in the NVPF electrode material. Another important aspect to consider is online parameter identification, estimation, and life prediction using the developed P2D model.

Declaration of Competing Interest

The authors declare that they have no known competing financial interests or personal relationships that could have appeared to influence the work reported in this paper.

Credit authorship contribution statement

Kudakwashe Chayambuka: Investigation, Software, Writing – original draft. **Grietus Mulder:** Supervision, Writing – review & editing. **Dmitri L. Danilov:** Supervision, Software, Writing – review & editing. **Peter H.L. Notten:** Resources, Supervision, Writing – review & editing.

Acknowledgments

D.L.D. has received funding from the European Union's Horizon 2020 Research and Innovation Program under Grant Agreement No. 769900-DEMOBASE. K.C. and G.M. are grateful for the support from the European Union's Horizon 2020 Research and Innovation Program under Grant Agreement No. 646433-NAIADES. KC highly appreciates support from the Living Lab Energy Campus (LLEC) at the Forschungszentrum Jülich.

Supplementary materials

Supplementary material associated with this article can be found, in the online version, at doi:10.1016/j.electacta.2021.139764.

Appendix A. Model parameters

This section lists the parameters used in the model and compares them to the experimental values where available.

Figs. A1 and A2 compare the concentration-dependent parameters, $D_{1,m}$ and k_m obtained from the P2D GITT model (symbols) [34] to the parameters used in the optimized full cell P2D model (solid line). In all cases, the obtained full cell model parameters are higher than the P2D GITT model parameters, although the same qualitative trend is maintained. These differences could be the result of model uncertainties and/or temperature effects at high discharge rates since the P2D GITT model parameters are obtained at comparatively very low currents (approximately C/30).

Fig. A3 compares the electrolyte properties, D_2 and κ obtained from the AEM version 2.19.1 (symbols) to the optimized parameters from the full cell P2D model (solid line). The values of κ were the same in both cases. Additional experimental measurements have validated the AEM electrolyte conductivity results [39].

Table A1
Parameters used in the model.

Parameter	Unit	Description	value	Reference
δ_n	[µm]	Anode thickness	64	[27]
δ_p	[µm]	Cathode thickness	68	[27]
δ_s	[µm]	Separator thickness	25	[27]
R_n	[µm]	HC particle radius	3.48	[27]
R_p	[µm]	NVPF particle radius	0.59	[27]
A_{cc}	[cm^2]	Electrode cross-section area	2.54	[27]
T	[K]	Cell temperature	298.15	[27]
$c_{1,n}^{max}$	[kmol m^{-3}]	HC max. concentration	14.54	[27]
$c_{1,p}^{max}$	[kmol m^{-3}]	NVPF max. concentration	15.32	[27]
$c_{1,n}^{0}$	[kmol m^{-3}]	HC initial concentration	14.52	[27]
$c_{1,p}^{0}$	[kmol m^{-3}]	NVPF initial concentration	3.32	[27]
c_2^0	[kmol m^{-3}]	$NaPF_6$ initial concentration	1	[27]
α	[-]	Charge transfer coefficient	0.5	optimization
t_+	[-]	Transference number	0.45	[39]
σ_n^{eff}	[Ω^{-1} m^{-1}]	Anode conductivity	256	optimization
σ_p^{eff}	[Ω^{-1} m^{-1}]	Cathode conductivity	50	optimization
ε_n^{el}	[-]	Electrolyte volume fraction in anode	0.51	optimization
ε_p^{el}	[-]	Electrolyte volume fraction in cathode	0.23	optimization
ε_s^{el}	[-]	Electrolyte volume fraction in separator	0.55	[65]
ε_n^{filler}	[-]	Filler volume fraction	0.001	optimization
ε_p^{filler}	[-]	Filler volume fraction	0.22	optimization
$R_{contact,n}$	[mΩ m^2]	Contract resistance	2	[27]
$R_{contact,p}$	[mΩ m^2]	Contract resistance	8.5	[27]

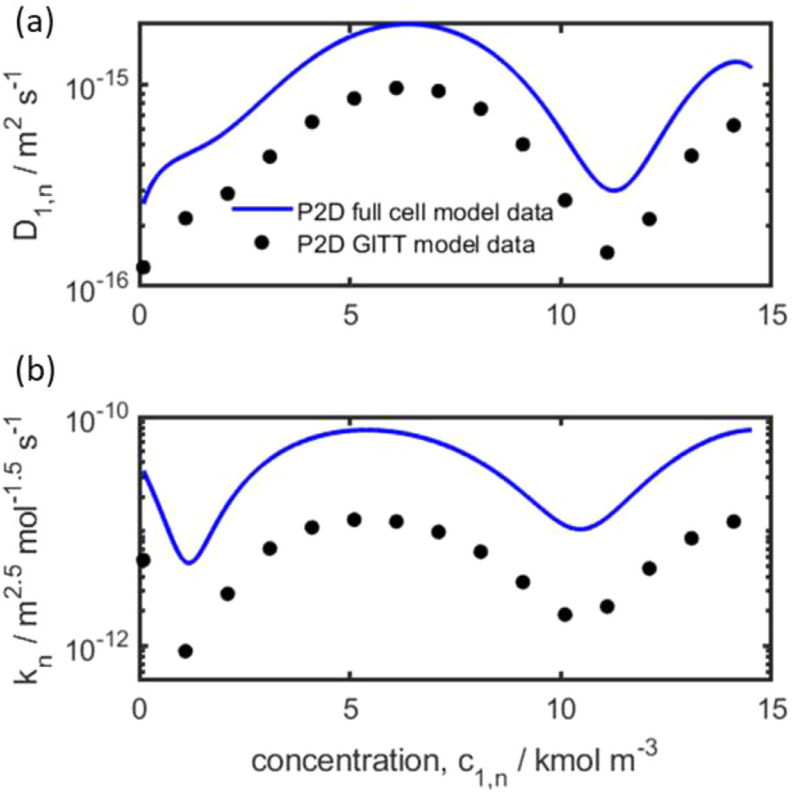

Fig. A1. HC electrode parameters from the P2D GITT model (symbols) and from the optimized full cell P2D model (solid line) as function of the intercalated Na^+ concentration, $c_{1,n}$. The diffusion coefficient in HC, $D_{1,n}$ (a) and the kinetic rate constant, k_n (b).

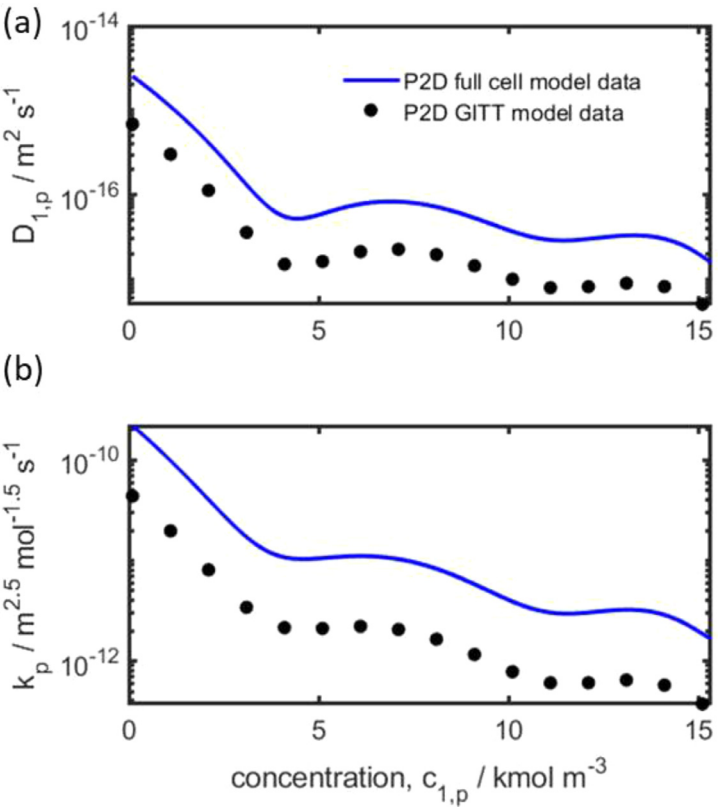

Fig. A2. NVPF positive electrode parameters from the P2D GITT model (symbols) and from the optimized full cell P2D model (solid line) as function of the intercalated Na^+ concentration, $c_{1,p}$. The diffusion coefficient in NVPF, $D_{1,p}$ (a) and kinetic rate constant, k_n (b).

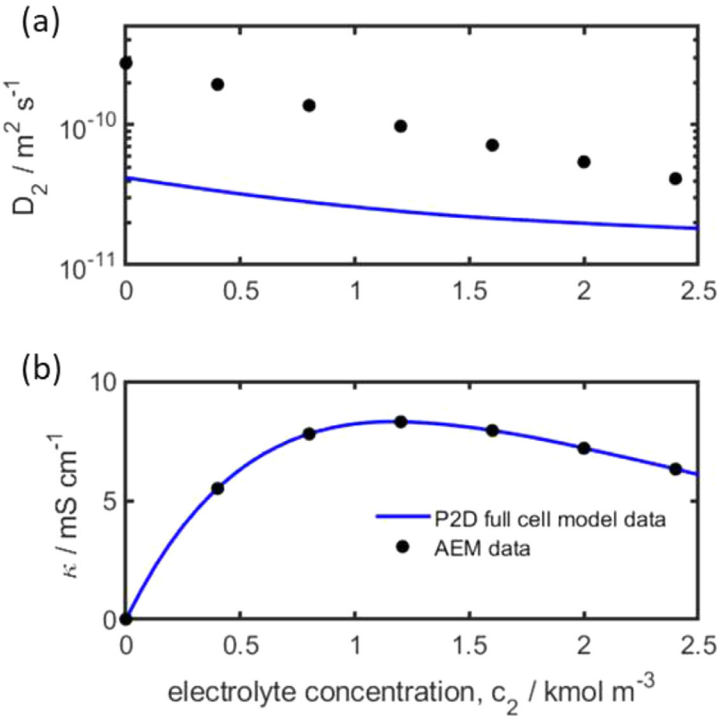

Fig. A3. Electrolyte properties of $NaPF_6$ salt dissolved in $EC_{0.5}$: $PC_{0.5}$ (w/w) solvent from the AEM (symbols) and from the optimized P2D model (solid line) as function of the salt concentration, c_2. The diffusion coefficient in the electrolyte, D_2 (a) and the electrolyte conductivity, κ (b).

However, the D_2 values used in the optimized P2D model are qualitatively similar but quantitatively lower than the ones obtained from the AEM. Because two models are used to determine these parameters, further experimental investigations are necessary to investigate the origin of the differences.

References

[1] K. Chayambuka, G. Mulder, D.L. Danilov, P.H.L. Notten, From Li-Ion Batteries toward Na-Ion Chemistries: challenges and Opportunities, Adv. Energy Mater. 10 (2020) 2001310, doi:10.1002/aenm.202001310.

[2] J.-.M. Tarascon, Na-ion versus Li-ion Batteries: complementarity Rather than Competitiveness, Joule 4 (2020) 1616–1620, doi:10.1016/j.joule.2020.06.003.

[3] K. Chayambuka, G. Mulder, D.L. Danilov, P.H.L. Notten, Sodium-Ion Battery Materials and Electrochemical Properties Reviewed, Adv. Energy Mater. 8 (2018) 1800079, doi:10.1002/aenm.201800079.

[4] N. Yabuuchi, K. Kubota, M. Dahbi, S. Komaba, Research Development on Sodium-Ion Batteries, Chem. Rev. 114 (2014) 11636–11682, doi:10.1021/cr500192f.

[5] J.-.Y. Hwang, S.-.T. Myung, Y.-.K. Sun, Sodium-ion batteries: present and future, Chem. Soc. Rev. 46 (2017) 3529–3614, doi:10.1039/C6CS00776G.

[6] C. Grosjean, P.H. Miranda, M. Perrin, P. Poggi, Assessment of world lithium resources and consequences of their geographic distribution on the expected development of the electric vehicle industry, Renew. Sustain. Energy Rev. 16 (2012) 1735–1744, doi:10.1016/j.rser.2011.11.023.

[7] B. Nykvist, F. Sprei, M. Nilsson, Assessing the progress toward lower priced long range battery electric vehicles, Energy Policy 124 (2019) 144–155, doi:10.1016/j.enpol.2018.09.035.

[8] H.S. Hirsh, Y. Li, D.H.S. Tan, M. Zhang, E. Zhao, Y.S. Meng, Sodium-Ion Batteries Paving the Way for Grid Energy Storage, Adv. Energy Mater. 10 (2020) 2001274, doi:10.1002/aenm.202001274.

[9] K. West, T. Jacobsen, S. Atlung, Modeling of Porous Insertion Electrodes with Liquid Electrolyte, J. Electrochem. Soc. 129 (1982) 1480–1485, doi:10.1149/1.2124188.

[10] B. Scrosati, Lithium Rocking Chair Batteries: an Old Concept? J. Electrochem. Soc. 139 (1992) 2776–2781, doi:10.1149/1.2068978.

[11] J. Newman, W. Tiedemann, Porous-electrode theory with battery applications, AIChE J. 21 (1975) 25–41, doi:10.1002/aic.690210103.

[12] C.M. Doyle, Design and Simulation of Lithium Rechargeable Batteries, Lawrence Berkeley National Laboratory., 1995 http://escholarship.org/uc/item/6j87z0sp (accessed April 11, 2017).

[13] T.F. Fuller, M. Doyle, J. Newman, Simulation and Optimization of the Dual Lithium Ion Insertion Cell, J. Electrochem. Soc. 141 (1994) 1–10, doi:10.1149/1.2054684.

[14] W.B. Gu, C.Y. Wang, B.Y. Liaw, Numerical Modeling of Coupled Electrochemical and Transport Processes in Lead-Acid Batteries, J. Electrochem. Soc. 144 (1997) 2053, doi:10.1149/1.1837741.

[15] B. Paxton, J. Newman, Modeling of nickel/metal hydride batteries, J. Electrochem. Soc. 144 (1997) 3818–3831, doi:10.1149/1.1838098.

[16] W. Li, D. Cao, D. Jöst, F. Ringbeck, M. Kuipers, F. Frie, D.U. Sauer, Parameter sensitivity analysis of electrochemical model-based battery management systems for lithium-ion batteries, Appl. Energy 269 (2020) 115104, doi:10.1016/j.apenergy.2020.115104.

[17] K.A. Smith, C.D. Rahn, C.-Y. Wang, Control oriented 1D electrochemical model of lithium ion battery, Energy Convers. Manag. 48 (2007) 2565–2578. https://doi.org/10.1016/j.enconman.2007.03.015.

[18] M. Guo, G. Sikha, R.E. White, Single-Particle Model for a Lithium-Ion Cell: thermal Behavior, J. Electrochem. Soc. 158 (2010) A122, doi:10.1149/1.3521314.

[19] J.M. Reniers, G. Mulder, S. Ober-Blöbaum, D.A. Howey, Optimal control of grid-connected li-ion batteries to maximise revenue and minimise degradation, Meet. Abstr. MA2017-02 40 (2017), doi:10.1149/MA2017-02/1/40.

[20] S.J. Moura, F.B. Argomedo, R. Klein, A. Mirtabatabaei, M. Krstic, Battery state estimation for a single particle model with electrolyte dynamics, IEEE Trans. Control Syst. Technol. 25 (2017) 453–468, doi:10.1109/TCST.2016.2571663.

[21] X. Lai, Y. Zheng, T. Sun, A comparative study of different equivalent circuit models for estimating state-of-charge of lithium-ion batteries, Electrochim. Acta 259 (2018) 566–577, doi:10.1016/j.electacta.2017.10.153.

[22] B. Yann Liaw, G. Nagasubramanian, R.G. Jungst, D.H. Doughty, Modeling of lithium ion cells—a simple equivalent-circuit model approach, Solid State Ionics 175 (2004) 835–839, doi:10.1016/j.ssi.2004.09.049.

[23] M. Schimpe, M.E. von Kuepach, M. Naumann, H.C. Hesse, K. Smith, A. Jossen, Comprehensive modeling of temperature-dependent degradation mechanisms in lithium iron phosphate batteries, J. Electrochem. Soc. 165 (2018) A181, doi:10.1149/2.1181714jes.

[24] K.A. Severson, P.M. Attia, N. Jin, N. Perkins, B. Jiang, Z. Yang, M.H. Chen, M. Aykol, P.K. Herring, D. Fraggedakis, M.Z. Bazant, S.J. Harris, W.C. Chueh, R.D. Braatz, Data-driven prediction of battery cycle life before capacity degradation, Nat. Energy 4 (2019) 383–391, doi:10.1038/s41560-019-0356-8.

[25] B. Wu, W.D. Widanage, S. Yang, X. Liu, Battery digital twins: perspectives on the fusion of models, data and artificial intelligence for smart battery management systems, Energy AI 1 (2020) 100016, doi:10.1016/j.egyai.2020.100016.

[26] A. Jokar, B. Rajabloo, M. Désilets, M. Lacroix, Review of simplified Pseudo-two-Dimensional models of lithium-ion batteries, J. Power Sources 327 (2016) 44–55, doi:10.1016/j.jpowsour.2016.07.036.

[27] K. Chayambuka, M. Jiang, G. Mulder, D.L. Danilov, P.H.L. Notten, Physics-based Modeling of Sodium-ion Batteries Part I: Experimental parameter determination, Electrochim. Acta (2021), doi:10.1016/j.electacta.2021.139726.

[28] Y. Cai, X. Cao, Z. Luo, G. Fang, F. Liu, J. Zhou, A. Pan, S. Liang, Caging Na3V2(PO4)2F3 Microcubes in Cross-Linked Graphene Enabling Ultrafast Sodium Storage and Long-Term Cycling, Adv. Sci. 5 (2018) 1800680, doi:10.1002/advs.201800680.

[29] Z.-.Y. Gu, J.-.Z. Guo, Z.-.H. Sun, X.-.X. Zhao, W.-.H. Li, X. Yang, H.-.J. Liang, C.-.D. Zhao, X.-.L. Wu, Carbon-coating-increased working voltage and energy density towards an advanced Na3V2(PO4)2F3@C cathode in sodium-ion batteries, Sci. Bull. 65 (2020) 702–710, doi:10.1016/j.scib.2020.01.018.

[30] K. Chayambuka, G. Mulder, D.L. Danilov, P.H.L. Notten, A modified pseudo-steady-state analytical expression for battery modeling, Solid State Commun. 296 (2019) 49–53, doi:10.1016/j.ssc.2019.04.011.

[31] H.S. Carslaw, J.C. Jaeger, Conduction of Heat in Solids, Oxford Science Publications, Oxford, England, 1959.

[32] R.A. Shakoor, D.-.H. Seo, H. Kim, Y.-.U. Park, J. Kim, S.-.W. Kim, H. Gwon, S. Lee, K. Kang, A combined first principles and experimental study on Na 3V 2 (PO 4) 2 F 3 for rechargeable Na batteries, J. Mater. Chem. 22 (2012) 20535–20541, doi:10.1039/C2JM33862A.

[33] Z. Liu, Y.-.Y. Hu, M.T. Dunstan, H. Huo, X. Hao, H. Zou, G. Zhong, Y. Yang, C.P. Grey, Local Structure and Dynamics in the Na Ion Battery Positive Electrode Material Na3V2(PO4)2F3, Chem. Mater. 26 (2014) 2513–2521, doi:10.1021/cm403728w.

[34] K. Chayambuka, G. Mulder, D.L. Danilov, P.H.L. Notten, Determination of state-of-charge dependent diffusion coefficients and kinetic rate constants of phase changing electrode materials using physics-based models, J. Power Sources Adv. 9 (2021) 100056, doi:10.1016/j.powera.2021.100056.

[35] K. Chayambuka, G. Mulder, D.L. Danilov, P.H.L. Notten, A hybrid backward euler control volume method to solve the concentration-dependent solid-state diffusion problem in battery modeling, J. Appl. Math. Phys. 8 (2020) 1066–1080, doi:10.4236/jamp.2020.86083.

[36] D. Danilov, R.aA.H. Niessen, P.H.L. Notten, Modeling all-solid-state Li-ion batteries, J. Electrochem. Soc. 158 (2010) A215, doi:10.1149/1.3521414.

[37] M.K. Das, P.P. Mukherjee, K. Muralidhar, Modeling Transport Phenomena in Porous Media With Applications, Springer, 2017.

[38] J. Newman, K.E. Thomas-Alyea, Electrochemical Systems, John Wiley & Sons, 2012.

[39] K. Chayambuka, R. Cardinaels, K.L. Gering, L.H.J. Raijmakers, G. Mulder, D.L. Danilov, P.H.L. Notten, An experimental and modeling study of sodium-ion battery electrolytes, J. Power Sources 516 (2021), doi:10.1016/j.jpowsour.2021.230658.

[40] D. Danilov, P.H.L. Notten, Mathematical modelling of ionic transport in the electrolyte of Li-ion batteries, Electrochim. Acta 53 (2008) 5569–5578, doi:10.1016/j.electacta.2008.02.086.

[41] R. Ranom, Mathematical Modelling of Lithium ion Batteries, University of Southampton, 2014.

[42] D.A.G. Bruggeman, Berechnung verschiedener physikalischer Konstanten von heterogenen Substanzen. I. Dielektrizitätskonstanten und Leitfähigkeiten der Mischkörper aus isotropen Substanzen, Ann. Phys. 416 (1935) 636–664, doi:10.1002/andp.19354160705.

[43] K.L. Gering, Prediction of electrolyte viscosity for aqueous and non-aqueous systems: results from a molecular model based on ion solvation and a chemical physics framework, Electrochim. Acta 51 (2006) 3125–3138, doi:10.1016/j.electacta.2005.09.011.

[44] K.L. Gering, Prediction of Electrolyte Conductivity: results from a Generalized Molecular Model Based on Ion Solvation and a Chemical Physics Framework, Electrochim. Acta 225 (2017) 175–189, doi:10.1016/j.electacta.2016.12.083.

[45] E.R. Logan, E.M. Tonita, K.L. Gering, L. Ma, M.K.G. Bauer, J. Li, L.Y. Beaulieu, J.R. Dahn, A study of the transport properties of ethylene carbonate-free Li electrolytes, J. Electrochem. Soc. 165 (2018) A705, doi:10.1149/2.0981803jes.

[46] S. Patankar, Numerical Heat Transfer and Fluid Flow, CRC press, 2018.

[47] G.G. Botte, V.R. Subramanian, R.E. White, Mathematical modeling of secondary lithium batteries, Electrochim. Acta 45 (2000) 2595–2609, doi:10.1016/S0013-4686(00)00340-6.

[48] G.G. Botte, J.A. Ritter, R.E. White, Comparison of finite difference and control volume methods for solving differential equations, Comput. Chem. Eng. 24 (2000) 2633–2654, doi:10.1016/S0098-1354(00)00619-0.

[49] Numerical Methods for Partial Differential Equations | ScienceDirect, (n.d.). https://www.sciencedirect.com/book/9780128498941/numerical-methods-for-partial-differential-equations#book-info (accessed April 21, 2021).

[50] A nonlinear shooting method for two-point boundary value problems, Comput. Math. Appl. 42 (2001) 1411–1420, doi:10.1016/S0898-1221(01)00250-4.

[51] A. Granas, R. Guenther, J. Lee, Nonlinear boundary value problems for ordinary differential equations, (1985). https://eudml.org/doc/268365 (accessed March 5, 2021).

[52] D.J. Wilde, Optimum Seeking Methods, Prentice-Hall, Englewood Cliffs, NJ, 1964 https://cds.cern.ch/record/268656 (accessed March 5, 2021).

[53] D.E. Stephenson, E.M. Hartman, J.N. Harb, D.R. Wheeler, Modeling of particle-particle interactions in porous cathodes for lithium-ion batteries, J. Electrochem. Soc. 154 (2007) A1146–A1155.

[54] A. Chipperfield, P. Fleming, H. Pohlheim, A genetic algorithm toolbox for MATLAB, in: Proceedings of the International Conference on Systems Engineering, 1994, pp. 200–207.

[55] T. Broux, F. Fauth, N. Hall, Y. Chatillon, M. Bianchini, T. Bamine, J.-.B. Leriche, E. Suard, D. Carlier, Y. Reynier, L. Simonin, C. Masquelier, L. Croguennec, High Rate Performance for Carbon-Coated Na3V2(PO4)2F3 in Na-Ion Batteries, Small Methods 3 (2019) 1800215, doi:10.1002/smtd.201800215.
[56] J. Newman, Optimization of porosity and thickness of a battery electrode by means of a reaction-zone model, J. Electrochem. Soc. 142 (1995) 97, doi:10.1149/1.2043956.
[57] M. Doyle, J. Newman, The use of mathematical modeling in the design of lithium/polymer battery systems, Electrochim. Acta 40 (1995) 2191–2196, doi:10.1016/0013-4686(95)00162-8.
[58] S. De, P.W.C. Northrop, V. Ramadesigan, V.R. Subramanian, Model-based simultaneous optimization of multiple design parameters for lithium-ion batteries for maximization of energy density, J. Power Sources 227 (2013) 161–170, doi:10.1016/j.jpowsour.2012.11.035.
[59] C. Miehe, H. Dal, L.-.M. Schänzel, A. Raina, A phase-field model for chemo-mechanical induced fracture in lithium-ion battery electrode particles, Int. J. Numer. Methods Eng. 106 (2016) 683–711, doi:10.1002/nme.5133.
[60] R.B. Smith, E. Khoo, M.Z. Bazant, Intercalation kinetics in multiphase-layered materials, J. Phys. Chem. C. 121 (2017) 12505–12523, doi:10.1021/acs.jpcc.7b00185.
[61] G.K. Singh, G. Ceder, M.Z. Bazant, Intercalation dynamics in rechargeable battery materials: general theory and phase-transformation waves in LiFePO4, Electrochim. Acta 53 (2008) 7599–7613, doi:10.1016/j.electacta.2008.03.083.
[62] S.F. Schneider, C. Bauer, P. Novák, E.J. Berg, A modeling framework to assess specific energy, costs and environmental impacts of Li-ion and Na-ion batteries, Sustain. Energy Fuels 3 (2019) 3061–3070, doi:10.1039/C9SE00427K.
[63] E. Berg, C. Villevieille, D. Streich, S. Trabesinger, P. Novak, Rechargeable batteries: grasping for the limits of chemistry, J. Electrochem. Soc. 162 (2015) A2468–A2475.
[64] G. Patry, A. Romagny, S. Martinet, D. Froelich, Cost modeling of lithium-ion battery cells for automotive applications, Energy Sci. Eng. 3 (2015) 71–82.
[65] New separator for PAT insulation sleeves | EL-CELL, (n.d.). https://el-cell.com/new-separator-for-pat-insulation-sleeves/(accessed March 5, 2021).